Determination of Viscoelastic Spectra by Matrix Eigenvalue Analysis

Ladislav Hanyk and Ctirad Matyska

Department of Geophysics, Faculty of Mathematics and Physics, Charles University, Prague, Czech Republic

David A. Yuen

University of Minnesota Supercomputing Institute and Department of Geology and Geophysics, Minneapolis

To appear in

`Ice Sheets, Sea Level and the Dynamic Earth,`
`ed. by J. X. Mitrovica and L. L. A. Vermeersen,`
`in press, AGU, 2002`

This study is devoted to the eigenvalue method for computing the normal modes of spherically symmetric self-gravitating viscoelastic Earth models. We employ the approach of the method of lines to the governing partial differential equations, i.e., we discretize the equations in space. This results in a system of time-dependent ordinary differential equations of the form $d\mathbf{Y}/dt = \boldsymbol{B}\mathbf{Y}$, which is fundamentally different from the modal approach where the time-dependence is dealt first. Using the finite differences in the grid space, we have conducted the eigenvalue analysis of the matrix $\boldsymbol{B}$, which yields simultaneously a full spectrum including the classical relaxation modes (M0, L0, C0), the stable dilatation modes and the unstable Rayleigh-Taylor modes. The Maxwell eigenvalues appear as a special class of degenerated modes with zero strength. However, there exists also a class of modes which are the by-products of the spatial discretization of the partial differential equations being investigated. Recognition of these discretization modes is easy due to their sensitivity to the particular kind of discretization employed, as well as the grid point density. The advantage of the eigenvalue procedure is that normal modes of realistic elastically compressible models with radially dependent viscosity profiles, which are characterized by complicated "continuous" relaxation spectra, can be found straightforwardly by a standard matrix eigenanalysis without transforming the problem to the tedious task of finding roots of a secular determinant in the Laplacian plane, which is the classical approach. Moreover, the computational speed of the eigenvalue method is extremely fast (of the order of a few seconds on current GHz processors for 100 radial grid points) and can be used for future work in nonlinear inversion. A series of numerical results starting from simple incompressible layered models and finishing with realistic PREM-based models with complicated viscosity profiles is presented.

1. INTRODUCTION

Geodynamic processes with short to intermediate timescales ranging from postseismic deformation from large earthquakes, on the period of months, to postglacial rebound, on the order of thousands of years, exhibit substantial deviation from elasticity due to both transient creep and viscoelastic processes [*Karato,* 1998]. For both anelastic and linear viscoelastic rheology, the normal mode approach can be applied in the same manner as for elastic free oscillations of the Earth by the correspondence principle [*Yuen and Peltier,* 1982]. The correspondence principle allows one to use the solution from the elastic problem with the Lamé parameters becoming dependent on the Laplacian variable s, depending on the particular type of rheology [*Christensen,* 1982]. This classical modal theory has remained the mainstay of the geophysical community, since it was introduced by *Peltier* [1974], because of its efficiency for simple models with layers of constant density, shear modulus and viscosity.

In the last several years, increased numerical difficulties have been encountered with more complex models where steep viscosity profiles have been introduced. E.g., *Hanyk et al.* [1995; 1996; 1998] showed numerically that finding even hundreds of modes need not lead to finding satisfactory accurate viscoelastic response and proposed a technique based on direct time-integration of ordinary differential equations. *Fang and Hager* [1995] dealt with viscosity profiles which vary continuously with depth due to the pressure dependence of mantle rheology. In some depth range the Laplace-transformed parameters become singular; to invert a response in the time domain without the effect of this singularity, they proposed a new integration contour in the complex Laplacian domain. *Spada et al.* [1992], *Wu and Ni* [1996] and *Boschi et al.* [1999] showed that the singular factors can be factorized from the analytically expressed secular determinant to prevent the occurrence of the Maxwell singularities. However, this regularization has been achieved only for layered incompressible models. *Han and Wahr* [1995] discussed the possibility of misinterpretation in finding modes by root-finding procedures of the secular determinant in the Laplacian domain due to false-zero crossings, referring to jumps between $\pm\infty$. Moreover, they also pointed to infinitely dense sets of modes in the Laplacian spectra of compressible models. In the case of the simplest layered models, these infinite set of compressible modes can be found analytically; there are not only the dilatation (D) modes, either stable [*Vermeersen et al.,* 1996] or unstable [*Vermeersen and Mitrovica,* 2000], but also

the unstable Rayleigh-Taylor (RT) modes [*Hanyk et al.,* 1999]. The unstable RT modes are also present in realistic continuously varying models with a subadiabatic gradient of density [*Plag and Jüttner,* 1995], such as the PREM [*Dziewonski and Anderson,* 1981]. Effects of a non-adiabatic density gradient on the gravitational stability of the viscoelastic responses have been studied by *Nakada* [1999].

Owing to the complicated nature of the normal mode spectrum for realistic Earth models with sharp variations of the elastic and viscous properties, the traditional approach of finding the roots to the secular determinant within the framework of the Laplacian domain becomes too cumbersome for using this in nonlinear inversion. Thus we need new numerical methods for this purpose. *Tromp and Mitrovica* [1999, 2000] presented a new normal-mode formalism, which is based upon eigenfunction expansions. However, relaxation times are still found by means of the clasical root-finding procedure, which can fail if the distance between neighbouring roots is infinitesimal, and is computationally expensive if a large number of modes should be found. *Hanyk et al.* [2000] have recently developed a new theoretical approach, which does not make use of the Laplacian transform. Instead, the problem is now cast as a matrix eigenvalue problem by discretizing the radial spatial variable. Such an eigenvalue approach in grid space allows one to employ the power of standard eigenvalue routines, which is a well-studied problem in numerical analysis. With this eigenvalue approach, we can easily obtain the whole spectrum in one fell swoop.

The aim of this study is to write all steps of this new theory in detail and to demonstrate its applicability to a variety of Earth models. In the next section we will formulate fundamental governing equations in the spatial-time domain as well as their discretization by means of spherical harmonics in the case of spherically symmetric models. The resultant two-dimensional partial differential equations (PDEs), with radius and time being the variables, can then be discretized in the radius, leaving a set of ordinary differential equations (ODEs) in time. Then we show that this system of ODEs can be solved by means of eigenvalue analysis from which we can retrieve both the spectra and the associated eigenvectors in the radial grid. The third section deals with the details concerning the relationships between the order of the finite-difference technique and the structure of the matrices, whose eigenvalues yield the complete set of relaxation times. We display the numerical results in the fourth section. We will first show that our technique provides precisely well-known

spectral groups for both incompressible and compressible layered models. We will concentrate on the problem of distinguishing relevant modes from those which are a result of radial discretization of rheology and density profiles. Lastly we show results from more realistic models with elastic parameters taken from the PREM and continuously varying viscosity profiles with variations of several orders of magnitude along the radius.

2. FORMULATION OF THE EIGENVALUE PROBLEM

2.1. PDEs in the 4-D Space-Time Domain

We consider a self-gravitating, compressible, non-rotating continuum initially in hydrostatic equilibrium. It is conventional to decompose total fields, such as the position vector, the stress tensor and the gravitational potential, into initial and incremental parts. The incremental fields are employed for description of infinitesimal, quasi-static, gravitational-viscoelastic perturbations of the initial fields. Physical quantities and PDEs given below conform to the standard form of gravitational viscoelastodynamics [*Peltier,* 1974], also referred to as the material-local form of the linearized field theory [*Wolf,* 1997].

The initial state of the continuum is described in terms of the initial Cauchy stress tensor $\boldsymbol{\tau}_0$, the initial gravitational potential φ_0, the initial density distribution ϱ_0 and the forcing term $\boldsymbol{f}_0$ by the momentum equation and the Poisson equation, respectively,

$$\nabla \cdot \boldsymbol{\tau}_0 + \boldsymbol{f}_0 = \boldsymbol{0}\,, \tag{1}$$

$$\nabla^2 \varphi_0 - 4\pi G \varrho_0 = 0\,, \tag{2}$$

where G is the Newton gravitational constant. We assume the initial stress to be hydrostatic, $\boldsymbol{\tau}_0 = -p_0 \boldsymbol{I}$, where p_0 denotes the mechanical pressure and $\boldsymbol{I}$ is the unit diagonal tensor, and identify the force $\boldsymbol{f}_0$ with the gravity force per unit volume, $\boldsymbol{f}_0 = -\rho_0 \nabla \varphi_0$. For the spherically symmetric density, $\varrho_0 = \varrho_0(r)$, eqn. (2) is reduced to

$$g_0' + 2g_0/r - 4\pi G \varrho_0 = 0\,, \tag{3}$$

where $g_0 \boldsymbol{e}_r = \nabla \varphi_0$ stands for the gravitational acceleration and the prime $'$ denotes differentiation with respect to r. The boundary conditions of the initial fields required at the surface and all internal boundaries are the continuity of the normal initial stress, the gravitational potential and the normal component of its gradient; moreover, the tangential stress vanishes at the surface and at liquid boundaries.

The incremental fields include the displacement $\mathbf{u}$, the incremental Cauchy stress tensor $\boldsymbol{\tau}$, the incremental gravitational potential φ_1 and the incremental density ϱ_1. For the incremental fields the adoption of the concept of Lagrangian or Eulerian formulations of a field becomes necessary, the former relating the current value of a field at the material point to its initial position, the latter relating the field to the current, local position. Leaving the derivation of the following equations for specialized monographs [e.g., *Wolf,* 1997], we assume that if $\boldsymbol{\tau}$ is in Lagrangian description and φ_1 and ϱ_1 are in Eulerian description, then within this rather conventional casting the momentum equation and the Poisson equation for infinitesimal, quasi-static perturbations will take the form

$$\nabla \cdot \boldsymbol{\tau} + \boldsymbol{f} = \mathbf{0}\,, \tag{4}$$

$$\nabla^2 \varphi_1 - 4\pi G \varrho_1 = 0\,, \tag{5}$$

where the forcing term $\boldsymbol{f}$ and the Eulerian incremental density ϱ_1 are

$$\boldsymbol{f} = -\varrho_0 \nabla \varphi_1 - \varrho_1 \nabla \varphi_0 - \nabla(\varrho_0 \mathbf{u} \cdot \nabla \varphi_0)\,, \tag{6}$$

$$\varrho_1 = -\nabla \cdot (\varrho_0 \mathbf{u})\,. \tag{7}$$

Introducing the dynamic viscosity η and the elastic Lamé parameters λ and μ, related to the bulk modulus K by $K = \lambda + \frac{2}{3}\mu$, the constitutive relation of the Maxwell rheology reads

$$\dot{\boldsymbol{\tau}} = \dot{\boldsymbol{\tau}^E} - \xi\left(\boldsymbol{\tau} - K \nabla \cdot \mathbf{u} \boldsymbol{I}\right)\,, \tag{8}$$

$$\boldsymbol{\tau}^E = \lambda \nabla \cdot \mathbf{u} \boldsymbol{I} + \mu \left[\nabla \mathbf{u} + (\nabla \mathbf{u})^T\right]\,, \tag{9}$$

$$\xi = \mu/\eta\,, \tag{10}$$

where the dots above letters denote differentiation with respect to time and the superscript ^{T} indicates the transpose operation. $\boldsymbol{\tau}^E$ is the auxiliary stress quantity formally identical to the elastic stress tensor; we introduce this symbol because of availability of spherical expansions of expressions with $\boldsymbol{\tau}^E$ which become necessary later. We note that other types of anelastic rheology, such as the standard linear solid or Burgers' body rheology [e.g., *Yuen and Peltier,* 1982] can be implemented in the same way as the Maxwell rheology, with suitable time-differentiation of the stress and strain tensors.

The internal boundary conditions for the incremental fields require continuity of the displacement, the incremental stress, the incremental gravitational potential and its gradient, $[\mathbf{u}]^+_- = \mathbf{0}$, $[\boldsymbol{\tau}]^+_- = \mathbf{0}$, $[\varphi_1]^+_- = 0$ and $[\nabla \varphi_1]^+_- = \mathbf{0}$, respectively. At liquid boundaries only zero tangential stress is required, $\boldsymbol{n} \cdot \boldsymbol{\tau} = (\boldsymbol{n} \cdot \boldsymbol{\tau} \cdot \boldsymbol{n})\boldsymbol{n}$, where

$\boldsymbol{n}$ is the unit vector normal to the boundaries; both radial and tangential displacements can be discontinuous. If the surface is loaded with the surface density γ_L, the surface boundary conditions for the incremental stress and the gradient of the incremental gravitational potential require the equilibrium with the load, $[\boldsymbol{n}\cdot\boldsymbol{\tau}]^+_- = -g_0\gamma_L\boldsymbol{n}$ and $[\boldsymbol{n}\cdot(\nabla\varphi_1 + 4\pi G\rho_0\mathbf{u})]^+_- = -4\pi G\gamma_L$.

The momentum equation (4) differentiated with respect to time, the Poisson equation (5) and the constitutive relation (8) can be combined into the system

$$\nabla\cdot\dot{\boldsymbol{\tau}}^E + \dot{\boldsymbol{f}} \;=\; \nabla\cdot\left[\xi\left(\boldsymbol{\tau} - K\nabla\cdot\mathbf{u}\boldsymbol{I}\right)\right]\,, \qquad (11)$$

$$\nabla\cdot(\nabla\varphi_1 + 4\pi G\varrho_0\mathbf{u}) \;=\; 0\,. \qquad (12)$$

This is where we drop the Laplacian approach based on the correspondence principle and start developing a new approach.

2.2. Spherical Harmonic Decomposition: PDEs in the 2-D Space-Time Domain

Now we proceed with converting PDEs (11)–(12), governing the response of the viscoelastic Earth mantle to a surface load, into sphericaly decomposed PDEs with respect to time and radius. We also summarize the relevant boundary and initial conditions. Hereafter we consider the spatial distribution of the parameters and the field variables as follows:

$$\begin{aligned}\varrho_0 = \varrho_0(r)\,,\ \lambda = \lambda(r)\,,\ \mu = \mu(r)\,,\ K = K(r)\,,\\ g_0 = g_0(r)\,,\quad \eta = \eta(r)\,,\quad \xi = \xi(r)\,,\\ \mathbf{u} = \mathbf{u}(r,\vartheta,\varphi)\,,\ \varphi_1 = \varphi_1(r,\vartheta,\varphi)\,,\ \boldsymbol{\tau} = \boldsymbol{\tau}(r,\vartheta,\varphi)\,.\end{aligned} \qquad (13)$$

Let $\boldsymbol{e}_r$, $\boldsymbol{e}_\vartheta$ and $\boldsymbol{e}_\varphi$ be the unit basis vectors of the spherical coordinates r, ϑ and φ, denoting radius, colatitude and longitude, respectively. We now introduce the definitions for the Legendre polynomials $P_n(x)$, the associated Legendre functions $P_n^m(x)$ and the scalar spherical harmonics $Y_{nm}(\vartheta,\varphi)$,

$$\begin{aligned}P_n(x) &= \tfrac{1}{2^n n!}\tfrac{d^n}{dx^n}(x^2-1)^n\,,\\ P_n^m(x) &= (1-x^2)^{\frac{m}{2}}\tfrac{d^m}{dx^m}P^n(x)\,,\\ Y_{nm}(\vartheta,\varphi) &= (-1)^m\sqrt{\tfrac{2n+1}{4\pi}\tfrac{(n-m)!}{(n+m)!}}P_n^m(\cos\vartheta)e^{im\varphi}\,.\end{aligned} \qquad (14)$$

We define orthogonal vector spherical harmonics $\boldsymbol{S}_{nm}^{(-1)}$, $\boldsymbol{S}_{nm}^{(1)} \equiv \nabla_\Omega Y_{nm}$ and $\boldsymbol{S}_{nm}^{(0)} \equiv \boldsymbol{e}_r\times\nabla_\Omega Y_{nm}$, where ∇_Ω is the tangential gradient operator, which is consistent with the Helmholtz representation of vector fields by the relations [e.g., *Dahlen and Tromp,* 1998]

$$\begin{aligned}\boldsymbol{S}_{nm}^{(-1)}(\vartheta,\varphi) &= Y_{nm}\boldsymbol{e}_r\,,\\ \boldsymbol{S}_{nm}^{(1)}(\vartheta,\varphi) &= \partial_\vartheta Y_{nm}\boldsymbol{e}_\vartheta + (\sin\vartheta)^{-1}\partial_\varphi Y_{nm}\boldsymbol{e}_\varphi\,,\\ \boldsymbol{S}_{nm}^{(0)}(\vartheta,\varphi) &= -(\sin\vartheta)^{-1}\partial_\varphi Y_{nm}\boldsymbol{e}_\vartheta + \partial_\vartheta Y_{nm}\boldsymbol{e}_\varphi\,.\end{aligned} \qquad (15)$$

The notation and normalization of the vector spherical harmonics has been chosen to conform with *Martinec* [1999]. In the space of square-integrable vector functions defined on the unit sphere, $\boldsymbol{S}^{(-1)}_{nm}$ and $\boldsymbol{S}^{(1)}_{nm}$ form the spheroidal basis, whereas $\boldsymbol{S}^{(0)}_{nm}$ create the toroidal basis.

We begin with spherical harmonic expansions of the following scalar and vector functions [cf. *Backus,* 1967]:

$$\begin{aligned}
\mathbf{u}(t,\boldsymbol{r}) &= \textstyle\sum_{nm}\big[U_{nm}(t,r)\boldsymbol{S}^{(-1)}_{nm} && (16)\\
&+ V_{nm}(t,r)\boldsymbol{S}^{(1)}_{nm} + W_{nm}(t,r)\boldsymbol{S}^{(0)}_{nm}\big]\,,\\
\varphi_1(t,\boldsymbol{r}) &= \textstyle\sum_{nm}\ F_{nm}(t,r)Y_{nm}\,, && (17)\\
\nabla\cdot\mathbf{u}(t,\boldsymbol{r}) &= \textstyle\sum_{nm}\ X_{nm}(t,r)Y_{nm}\,, && (18)\\
\boldsymbol{T}_r(t,\boldsymbol{r}) &= \textstyle\sum_{nm}\big[T_{rr,nm}(t,r)\boldsymbol{S}^{(-1)}_{nm} && (19)\\
&+ T_{r\vartheta,nm}(t,r)\boldsymbol{S}^{(1)}_{nm} + T_{r\varphi,nm}(t,r)\boldsymbol{S}^{(0)}_{nm}\big]\,,\\
\boldsymbol{T}^E_r(t,\boldsymbol{r}) &= \textstyle\sum_{nm}\big[T^E_{rr,nm}(t,r)\boldsymbol{S}^{(-1)}_{nm} && (20)\\
&+ T^E_{r\vartheta,nm}(t,r)\boldsymbol{S}^{(1)}_{nm} + T^E_{r\varphi,nm}(t,r)\boldsymbol{S}^{(0)}_{nm}\big]\,,
\end{aligned}$$

where t denotes time and $\boldsymbol{T}_r \equiv \boldsymbol{e}_r\cdot\boldsymbol{\tau}$ and $\boldsymbol{T}^E_r \equiv \boldsymbol{e}_r\cdot\boldsymbol{\tau}^E$ are the radial stress vectors connected by the relation

$$\dot{\boldsymbol{T}}_r \;=\; \dot{\boldsymbol{T}}^E_r - \xi\left(\boldsymbol{T}_r - K\nabla\cdot\mathbf{u}\,\boldsymbol{e}_r\right)\,, \qquad (21)$$

that follows from (8). The coefficients satisfy the relations

$$\begin{aligned}
X_{nm} &= U'_{nm} + (2U_{nm} - NV_{nm})/r\,, && (22)\\
T^E_{rr,nm} &= \lambda X_{nm} + 2\mu U'_{nm} && (23)\\
&= \beta U'_{nm} + \lambda(2U_{nm} - NV_{nm})/r\,,\\
T^E_{r\vartheta,nm} &= \mu V'_{nm} + \mu(U_{nm} - V_{nm})/r\,, && (24)\\
T^E_{r\varphi,nm} &= \mu(W'_{nm} - W_{nm}/r)\,, && (25)
\end{aligned}$$

with $\beta = \lambda + 2\mu$, $\gamma = \mu(3\lambda + 2\mu)/\beta$ and $N = n(n+1)$, and an auxiliary coefficient Q_{nm} is defined by

$$Q_{nm} \;=\; F'_{nm} + (n+1)F_{nm}/r + 4\pi G\varrho_0 U_{nm}\,. \qquad (26)$$

The prime $'$ denotes differentiation with respect to r. Making use of these coefficients, we can write the other necessary spherical harmonic expansions [cf. *Martinec,* 1999],

$$\begin{aligned}
\nabla\cdot\boldsymbol{\tau}^E \;=\; &\textstyle\sum_{nm}\Big[\big(T^{E\,\prime}_{rr,nm} - \frac{4\gamma}{r^2}U_{nm} + \frac{2N\gamma}{r^2}V_{nm}\\
&+ \tfrac{4\mu}{r\beta}T^E_{rr,nm} - \tfrac{N}{r}T^E_{r\vartheta,nm}\big)\boldsymbol{S}^{(-1)}_{nm} + \big(T^{E\,\prime}_{r\vartheta,nm}\\
&+ \tfrac{2\gamma}{r^2}U_{nm} - \tfrac{N\gamma+(N-2)\mu}{r^2}V_{nm} + \tfrac{\lambda}{r\beta}T^E_{rr,nm}\\
&+ \tfrac{3}{r}T^E_{r\vartheta,nm}\big)\boldsymbol{S}^{(1)}_{nm} + \big(T^{E\,\prime}_{r\varphi,nm} - \tfrac{(N-2)\mu}{r^2}W_{nm}\\
&+ \tfrac{3}{r}T^E_{r\varphi,nm}\big)\boldsymbol{S}^{(0)}_{nm}\Big]\,, \qquad (27)
\end{aligned}$$

$$\begin{aligned}\boldsymbol{f} &= \textstyle\sum_{nm}\Big[\big(\frac{4\varrho_0 g_0}{r}U_{nm} - \frac{N\varrho_0 g_0}{r}V_{nm} + \frac{(n+1)\varrho_0}{r}F_{nm} \\ &- \varrho_0 Q_{nm}\big)\boldsymbol{S}^{(-1)}_{nm} - \big(\frac{\varrho_0 g_0}{r}U_{nm} + \frac{\varrho_0}{r}F_{nm}\big)\boldsymbol{S}^{(1)}_{nm}\Big]\,, \quad (28)\\ \nabla\cdot(\nabla\varphi_1 + 4\pi G\varrho_0\mathbf{u}) &= \textstyle\sum_{nm}\big[Q'_{nm} - \frac{n-1}{r}Q_{nm} \\ &+ 4\pi G\frac{(n+1)\varrho_0}{r}U_{nm} - 4\pi G\frac{N\varrho_0}{r}V_{nm}\Big]Y_{nm}\,. \quad (29)\end{aligned}$$

From the coefficients of the spherical harmonic expansions of $\mathbf{u}$, φ_1, $\boldsymbol{\tau}$ and $\boldsymbol{\tau}^E$ we construct the 8-element vectors $\mathbf{y}_{nm}(t,r)$ and $\mathbf{y}^E_{nm}(t,r)$,

$$\begin{aligned}\mathbf{y}_{nm}(t,r) &= \big(U_{nm}, V_{nm}, T_{rr,nm}, T_{r\vartheta,nm}, \\ &\qquad F_{nm}, Q_{nm}, W_{nm}, T_{r\varphi,nm}\big)\,, \quad (30)\\ \mathbf{y}^E_{nm}(t,r) &= \big(U_{nm}, V_{nm}, T^E_{rr,nm}, T^E_{r\vartheta,nm}, \\ &\qquad F_{nm}, Q_{nm}, W_{nm}, T^E_{r\varphi,nm}\big)\,. \quad (31)\end{aligned}$$

As all the introduced spherical harmonic expansions are decoupled with respect to both degree n and order m, we suppress these subscripts hereafter. Elements of $\mathbf{y}$ and $\mathbf{y}^E$ can be trivially decomposed into the spheroidal (elements 1..6) and the toroidal (elements 7..8) parts; the spheroidal elements are ordered in accord with *Pelti-er* [1974]. We see that $\mathbf{y}$ differs from $\mathbf{y}^E$ only in the coefficients of the stress vectors $\boldsymbol{T}_r$ and $\boldsymbol{T}^E_r$ related by (21),

$$\begin{aligned}\dot y^E_1 &= \dot y_1\,, & \dot y^E_2 &= \dot y_2\,,\\ \dot y^E_3 &= \dot y_3 + \xi(y_3 - KX)\,, & \dot y^E_4 &= \dot y_4 + \xi y_4\,,\\ \dot y^E_5 &= \dot y_5\,, & \dot y^E_6 &= \dot y_6\,, \quad (32)\\ \dot y^E_7 &= \dot y_7\,, & \dot y^E_8 &= \dot y_8 + \xi y_8\,,\\ X &= y'_1 + (2y_1 - Ny_2)/r\,.\end{aligned}$$

First, we construct the PDEs for the coefficients (23)–(26). By substituting $\mathbf{y}^E$ into the above relations, we assemble four first-order PDEs in t and r,

$$\begin{aligned}y^{E\,\prime}_1 &= \textstyle\sum_k a_{1k} y^E_k\,, \quad (33)\\ a_{1,1..8} &= \big(-\frac{2\lambda}{r\beta}, \frac{N\lambda}{r\beta}, \frac{1}{\beta}, 0, 0, 0, 0, 0\big)\,,\\ y^{E\,\prime}_2 &= \textstyle\sum_k a_{2k} y^E_k\,, \quad (34)\\ a_{2,1..8} &= \big(-\frac{1}{r}, \frac{1}{r}, 0, \frac{1}{\mu}, 0, 0, 0, 0\big)\,,\\ y^{E\,\prime}_5 &= \textstyle\sum_k a_{5k} y^E_k\,, \quad (35)\\ a_{5,1..8} &= \big(-4\pi G\varrho_0, 0, 0, 0, -\frac{n+1}{r}, 1, 0, 0\big)\,,\\ y^{E\,\prime}_7 &= \textstyle\sum_k a_{7k} y^E_k\,, \quad (36)\\ a_{7,1..8} &= \big(0, 0, 0, 0, 0, 0, \frac{1}{r}, \frac{1}{\mu}\big)\,,\end{aligned}$$

with $\sum_k$ representing $\sum_{k=1}^{8}$. After differentiation in time and with the change of variables from $\mathbf{y}^E$ to $\mathbf{y}$

in accord with (32), we obtain four PDEs for elements of $\mathbf{y}$,

$$\begin{aligned}
&\dot{y}_1' - \textstyle\sum_k a_{1k}\dot{y}_k \;=\; \xi\,[a_{13}(y_3 - KX) && (37)\\
&\quad + a_{14}y_4 + a_{18}y_8] \;=\; \xi a_{13}(y_3 - KX)\,,\\
&\dot{y}_2' - \textstyle\sum_k a_{2k}\dot{y}_k \;= && (38)\\
&\quad = \xi\,[a_{23}(y_3 - KX) + a_{24}y_4 + a_{28}y_8] \;=\; \xi a_{24}y_4\,,\\
&\dot{y}_5' - \textstyle\sum_k a_{5k}\dot{y}_k \;= && (39)\\
&\quad = \xi\,[a_{53}(y_3 - KX) + a_{54}y_4 + a_{58}y_8] \;=\; 0\,,\\
&\dot{y}_7' - \textstyle\sum_k a_{7k}\dot{y}_k \;= && (40)\\
&\quad = \xi\,[a_{73}(y_3 - KX) + a_{74}y_4 + a_{78}y_8] \;=\; \xi a_{78}y_8\,,
\end{aligned}$$

where the zero terms have been discarded in the rightmost expressions. Second, we deal with the momentum equation (11). We start with rewriting (27)–(28) in terms of $\mathbf{y}^E$,

$$\begin{aligned}
\nabla\cdot\boldsymbol{\tau}^E \;&=\; \textstyle\sum_{nm}\big[\big(y_3^{E\,\prime} - \sum_k b_{3k}y_k^E\big)\,\boldsymbol{S}_{nm}^{(-1)} && (41)\\
&\quad + \big(y_4^{E\,\prime} - \textstyle\sum_k b_{4k}y_k^E\big)\,\boldsymbol{S}_{nm}^{(1)} + \big(y_8^{E\,\prime} - \textstyle\sum_k b_{8k}y_k^E\big)\,\boldsymbol{S}_{nm}^{(0)}\big]\,,\\
\boldsymbol{f} \;&=\; \textstyle\sum_{nm}\Big[-\sum_k c_{3k}y_k^E\,\boldsymbol{S}_{nm}^{(-1)} - \sum_k c_{4k}y_k^E\,\boldsymbol{S}_{nm}^{(1)}\Big]\,, && (42)
\end{aligned}$$

where the auxiliary coefficients b_{ik} and c_{ik} are given by

$$\begin{aligned}
b_{3,1..8} \;&=\; \big(\tfrac{4\gamma}{r^2}, -\tfrac{2N\gamma}{r^2}, -\tfrac{4\mu}{r\beta}, \tfrac{N}{r}, 0, 0, 0, 0\big) && (43)\\
b_{4,1..8} \;&=\; \big(-\tfrac{2\gamma}{r^2}, \tfrac{N\gamma+(N-2)\mu}{r^2}, -\tfrac{\lambda}{r\beta}, -\tfrac{3}{r}, 0, 0, 0, 0\big) && (44)\\
b_{8,1..8} \;&=\; \big(0, 0, 0, 0, 0, 0, \tfrac{(N-2)\mu}{r^2}, -\tfrac{3}{r}\big) && (45)\\
c_{3,1..8} \;&=\; \big(-\tfrac{4\varrho_0 g_0}{r}, \tfrac{N\varrho_0 g_0}{r}, 0, 0, -\tfrac{(n+1)\varrho_0}{r}, \varrho_0, 0, 0\big) && (46)\\
c_{4,1..8} \;&=\; \big(\tfrac{\varrho_0 g_0}{r}, 0, 0, 0, \tfrac{\varrho_0}{r}, 0, 0, 0\big)\,. && (47)
\end{aligned}$$

Then we differentiate (41)–(42) with respect to t, substitute $\mathbf{y}$ from (32) and discard the zero terms,

$$\begin{aligned}
\nabla\cdot\dot{\boldsymbol{\tau}}^E \;&=\; \textstyle\sum_{nm}[\dot{y}_3' + (\xi(y_3 - KX))']\\
&\quad - \quad \textstyle\sum_k b_{3k}\dot{y}_k - b_{33}\xi(y_3 - KX) - b_{34}\xi y_4]\boldsymbol{S}_{nm}^{(-1)}\\
&\quad + \quad \textstyle\sum_{nm}[\dot{y}_4' + (\xi y_4)']\\
&\quad - \quad \textstyle\sum_k b_{4k}\dot{y}_k - b_{43}\xi(y_3 - KX) - b_{44}\xi y_4]\boldsymbol{S}_{nm}^{(1)}\\
&\quad + \quad \textstyle\sum_{nm}[\dot{y}_8' + (\xi y_8)' - \sum_k b_{8k}\dot{y}_k - b_{88}\xi y_8]\boldsymbol{S}_{nm}^{(0)} && (48)\\
\dot{\boldsymbol{f}} \;&=\; \textstyle\sum_{nm}[-\sum_k c_{3k}\dot{y}_k\boldsymbol{S}_{nm}^{(-1)} - \sum_k c_{4k}\dot{y}_k\boldsymbol{S}_{nm}^{(1)}]\,. && (49)
\end{aligned}$$

For the right-hand side of (11) we can write

$$\begin{aligned}
&\nabla\cdot[\xi\,(\boldsymbol{\tau} - K\nabla\cdot\mathbf{u}\boldsymbol{I})] \;=\\
&\quad = \quad \xi\,[\nabla\cdot\boldsymbol{\tau} - \nabla(K\nabla\cdot\mathbf{u})] + \nabla\xi\cdot[\boldsymbol{\tau} - K\nabla\cdot\mathbf{u}\boldsymbol{I}]\\
&\quad = \quad \xi\,[-\boldsymbol{f} - \nabla(K\nabla\cdot\mathbf{u})] + \xi'\,[\boldsymbol{T}_r - K\nabla\cdot\mathbf{u}\boldsymbol{e}_r]\\
&\quad = \quad \textstyle\sum_{nm}\,[\xi\sum_k c_{3k}y_k - \xi(KX)' + \xi'(y_3 - KX)]\,\boldsymbol{S}_{nm}^{(-1)}\\
&\quad + \quad \textstyle\sum_{nm}\,[\xi\sum_k c_{4k}y_k - \xi KX/r + \xi' y_4]\,\boldsymbol{S}_{nm}^{(1)}\\
&\quad + \quad \textstyle\sum_{nm}\,[\xi' y_8]\,\boldsymbol{S}_{nm}^{(0)}\,. && (50)
\end{aligned}$$

Using (48)–(50), we obtain three first-order PDEs with respect to t and r from three scalar components of (11),

$$\begin{aligned}\dot{y}_3' - \textstyle\sum_k a_{3k}\dot{y}_k &= \xi[-y_3' + b_{33}(y_3 - KX) \\ &+ b_{34}y_4 + \textstyle\sum_k c_{3k}y_k] = \xi[-y_3' \\ &+ \textstyle\sum_k a_{3k}y_k - b_{31}y_1 - b_{32}y_2 - b_{33}KX]\,, \end{aligned} \tag{51}$$

$$\begin{aligned}\dot{y}_4' - \textstyle\sum_k a_{4k}\dot{y}_k &= \xi[-y_4' + b_{43}(y_3 - KX) \\ &+ b_{44}y_4 + \textstyle\sum_k c_{4k}y_k - KX/r] = \xi[-y_4' \\ &+ \textstyle\sum_k a_{4k}y_k - b_{41}y_1 - b_{42}y_2 - (b_{43} + 1/r)KX]\,, \end{aligned} \tag{52}$$

$$\begin{aligned}\dot{y}_8' - \textstyle\sum_k a_{8k}\dot{y}_k &= \xi[-y_8' + b_{88}y_8] = \xi[-y_8' \\ &+ \textstyle\sum_k a_{8k}y_k - b_{87}y_7]\,, \end{aligned} \tag{53}$$

where

$$a_{3,1..8} = b_{3,1..8} + c_{3,1..8}\,, \tag{54}$$

$$a_{4,1..8} = b_{4,1..8} + c_{4,1..8}\,, \tag{55}$$

$$a_{8,1..8} = b_{8,1..8}\,. \tag{56}$$

Third, we use the expansion in (29) and differentiate the Poisson equation (12) in time to obtain

$$\dot{y}_6' - \textstyle\sum_k a_{6k}\dot{y}_k = 0\,, \tag{57}$$

$$a_{6,1..8} = \left(-4\pi G\tfrac{(n+1)\varrho_0}{r}, 4\pi G\tfrac{N\varrho_0}{r}, 0, 0, 0, \tfrac{n-1}{r}, 0, 0\right).$$

We note that the analytical differentiation of the Poisson equation in time is not necessary because of its elliptic character. It turns out that it would correspond to index reduction, one of techniques of solving differential-algebraic equations [*Ascher and Petzold,* 1998].

With (37)–(40), (51)–(53), (57) and with the expression (22) for coefficients X, we arrive at the linear system of eight first-order PDEs with respect to t and r for the solution vector $\mathbf{y}$,

$$\begin{aligned}\dot{\mathbf{y}}'(t,r) - \boldsymbol{A}_n(r)\,\dot{\mathbf{y}}(t,r) &= \\ = \xi(r)\left[\boldsymbol{D}_n(r)\,\mathbf{y}'(t,r) + \boldsymbol{E}_n(r)\,\mathbf{y}(t,r)\right]&.\end{aligned} \tag{58}$$

System (58) is decoupled with respect to degree n, independent of order m, and for each n and m consists of two independent systems, one with 6×6 matrices (e.g., $a_{1..6,1..6}$), connecting the spheroidal coefficients of $\mathbf{u}$, φ_1 and $\boldsymbol{\tau}$, and the other one with 2×2 matrices (e.g., $a_{7..8,7..8}$), containing the toroidal coefficients. We can

express matrices $\boldsymbol{A}_n(r)$, $\boldsymbol{D}_n(r)$ and $\boldsymbol{E}_n(r)$ explicitly:

$$\boldsymbol{A}_n = \begin{pmatrix} -\frac{2\lambda}{r\beta} & \frac{N\lambda}{r\beta} & \frac{1}{\beta} \\ -\frac{1}{r} & \frac{1}{r} & 0 \\ \frac{4\gamma}{r^2} - \frac{4\varrho_0 g_0}{r} & -\frac{2N\gamma}{r^2} + \frac{N\varrho_0 g_0}{r} & -\frac{4\mu}{r\beta} \\ -\frac{2\gamma}{r^2} + \frac{\varrho_0 g_0}{r} & \frac{N\gamma + (N-2)\mu}{r^2} & -\frac{\lambda}{r\beta} \\ -4\pi G\varrho_0 & 0 & 0 \\ -4\pi G\frac{(n+1)\varrho_0}{r} & 4\pi G\frac{N\varrho_0}{r} & 0 \\ 0 & 0 & 0 \\ 0 & 0 & 0 \end{pmatrix}$$

$$\begin{pmatrix} 0 & 0 & 0 & 0 & 0 \\ \frac{1}{\mu} & 0 & 0 & 0 & 0 \\ \frac{N}{r} & -\frac{(n+1)\varrho_0}{r} & \varrho_0 & 0 & 0 \\ -\frac{3}{r} & \frac{\varrho_0}{r} & 0 & 0 & 0 \\ 0 & -\frac{n+1}{r} & 1 & 0 & 0 \\ 0 & 0 & \frac{n-1}{r} & 0 & 0 \\ 0 & 0 & 0 & \frac{1}{r} & \frac{1}{\mu} \\ 0 & 0 & 0 & \frac{(N-2)\mu}{r^2} & -\frac{3}{r} \end{pmatrix} \tag{59}$$

$$\boldsymbol{D}_n = \begin{pmatrix} -\frac{K}{\beta} & 0 & 0 & 0 & 0 & 0 & 0 & 0 \\ 0 & 0 & 0 & 0 & 0 & 0 & 0 & 0 \\ \frac{4\gamma}{3r} & 0 & -1 & 0 & 0 & 0 & 0 & 0 \\ -\frac{2\gamma}{3r} & 0 & 0 & -1 & 0 & 0 & 0 & 0 \\ 0 & 0 & 0 & 0 & 0 & 0 & 0 & 0 \\ 0 & 0 & 0 & 0 & 0 & 0 & 0 & 0 \\ 0 & 0 & 0 & 0 & 0 & 0 & 0 & 0 \\ 0 & 0 & 0 & 0 & 0 & 0 & 0 & -1 \end{pmatrix} \tag{60}$$

$$
\boldsymbol{E}_n \;=\; \left(\begin{array}{ccc}
-\dfrac{2K}{r\beta} & \dfrac{NK}{r\beta} & \dfrac{1}{\beta} \\
0 & 0 & 0 \\
\dfrac{8\gamma}{3r^2}-\dfrac{4\varrho_0 g_0}{r} & -\dfrac{4N\gamma}{3r^2}+\dfrac{N\varrho_0 g_0}{r} & -\dfrac{4\mu}{r\beta} \\
-\dfrac{4\gamma}{3r^2}+\dfrac{\varrho_0 g_0}{r} & \dfrac{2N\gamma}{3r^2} & -\dfrac{\lambda}{r\beta} \\
0 & 0 & 0 \\
0 & 0 & 0 \\
0 & 0 & 0 \\
0 & 0 & 0
\end{array}\right.
$$

$$
\left.\begin{array}{ccccc}
0 & 0 & 0 & 0 & 0 \\
\dfrac{1}{\mu} & 0 & 0 & 0 & 0 \\
\dfrac{N}{r} & -\dfrac{(n+1)\varrho_0}{r} & \varrho_0 & 0 & 0 \\
-\dfrac{3}{r} & \dfrac{\varrho_0}{r} & 0 & 0 & 0 \\
0 & 0 & 0 & 0 & 0 \\
0 & 0 & 0 & 0 & 0 \\
0 & 0 & 0 & 0 & \dfrac{1}{\mu} \\
0 & 0 & 0 & 0 & -\dfrac{3}{r}
\end{array}\right) . \qquad (61)
$$

We recall that for compressible Earth models, i.e., for finite values of K and λ, we have introduced the abbreviations $\beta = \lambda + 2\mu$, $\gamma = \mu(3\lambda + 2\mu)/\beta = 3\mu K/\beta$ and $N = n(n+1)$. For the incompressible models, $K \to \infty$, the expressions

$$
1/\beta \to 0\,, \quad \lambda/\beta \to 1\,, \quad \text{and} \quad \gamma \to 3\mu \qquad (62)
$$

should be substituted in (59)–(61).

In the limit of the elastic mantle, $\eta(r) \to \infty$ and $\xi(r) \to 0$, PDEs (58) should be consistent with the corresponding equations governing elastic free oscillations in the zero-frequency limit [e.g., *Dahlen and Tromp,* 1998, cf. (8.114)–(8.115) and (8.135)–(8.140)]. It can be found easily that these are satisfied. In the opposite limit of the inviscid mantle, $\eta(r) \to 0$ and $\xi(r) \to \infty$, we obtain the static PDEs

$$
\boldsymbol{D}_n \mathbf{y}'(r) + \boldsymbol{E}_n \mathbf{y}(r) \;=\; 0\,, \qquad (63)
$$

which can be shown to be equivalent with

$$
\mathbf{y}'(r) - \boldsymbol{A}_n \mathbf{y}(r) \;=\; 0\,, \qquad (64)
$$

where $\mu(r) \to 0$ is assumed in $\boldsymbol{A}_n(r)$. PDEs (64), governing the static deformation of the outer core, were discussed recently in, e.g., *Fang* [1998].

Finally, we summarize the valid boundary conditions at the surface, $r = a$, and at the core-mantle boundary, $r = b$, or at $r = 0$, if no liquid core is present in the model. Responses to an arbitrary surface load can be deduced from the response to a surface point mass load with the spherical harmonic representation expressed in the form $\gamma_L(t,\vartheta) = \sum_n \Gamma_n(t) P_{n0}(\cos\vartheta)$, where $\Gamma_n(t) = (2n+1)/(4\pi a^2) f(t)$ and $f(t)$ describes the time evolution of the load [*Farrell,* 1972]. The surface boundary conditions then can be written as

$$\begin{aligned} T_{rr}(t,a) &= -\left[4\pi/(2n+1)\right]^{\frac{1}{2}}\ g_0 \Gamma_n(t)\,, \\ T_{r\vartheta}(t,a) &= 0\,, \\ Q(t,a) &= -\left[4\pi/(2n+1)\right]^{\frac{1}{2}}\ 4\pi G \Gamma_n(t)\,, \\ T_{r\varphi}(t,a) &= 0\,, \end{aligned} \tag{65}$$

where the square-rooted terms are the normalization factors due to definition (14). Conditions at the centre of models without the liquid core, $r = b = 0$, require zero values for both the displacement and the incremental gravitational potential,

$$\begin{aligned} U(t,0) &= 0\,, \\ V(t,0) &= 0\,, \\ F(t,0) &= 0\,, \\ W(t,0) &= 0\,. \end{aligned} \tag{66}$$

For models with the liquid core the boundary conditions at the core-mantle boundary, $r = b > 0$, are according to, e.g., *Wu and Peltier* [1982],

$$\begin{aligned} -\varrho_0^- g_0 U(t,b) + T_{rr}(t,b) - \varrho_0^- F(t,b) &= 0\,, \\ T_{r\vartheta}(t,b) &= 0\,, \\ -4\pi G \varrho_0^- U(t,b) - (4\pi G \varrho_0^-/g_0 + C) F(t,b) &+ \\ + Q(t,b) &= 0\,, \\ T_{r\varphi}(t,b) &= 0\,, \end{aligned} \tag{67}$$

where ϱ_0^- is the density of the core at $r \to b$ and C is a constant defined as $C = Q^-/F^-$. F^- and Q^- are solutions at $r = b$ of ODEs governing the response of the incompressible inviscid core [*Wu and Peltier,* 1982],

$$\begin{pmatrix} F'(r) \\ Q'(r) \end{pmatrix} = \begin{pmatrix} \frac{4\pi G \varrho_0}{g_0} - \frac{n+1}{r} & 1 \\ \frac{8\pi G \varrho_0 (n-1)}{r g_0} & \frac{n-1}{r} - \frac{4\pi G \varrho_0}{g_0} \end{pmatrix} \begin{pmatrix} F(r) \\ Q(r) \end{pmatrix}. \tag{68}$$

This system is to be solved for the constant C only once by the integration from a point r_0 near the centre with the initial values $F(r_0) = r_0^n$ and $Q(r_0) = 2(n-1) r_0^{n-1}$.

For the load applied at $t = 0$ and kept in effect continuously for $t > 0$, i.e., for the Heaviside time dependence $f(t) = H(t)$, the Maxwell Earth model responds elastically at $t = 0$ and the appropriate initial condition for

$\mathbf{y}(t,r)$ thus requires

$$\mathbf{y}(0,r) \quad = \quad \mathbf{y}^E(r)\,. \tag{69}$$

The elastic solution $\mathbf{y}^E(r)$ can be computed from ODEs

$$\mathbf{y}^{E\,\prime}(r) \quad = \quad \boldsymbol{A}_n(r)\mathbf{y}^E(r) \tag{70}$$

again by the integration from the centre. However, explicit evaluation of $\mathbf{y}^E(r)$ is not necessary for the purpose of the present study.

In PDEs (58) and conditions (65)–(69) we arrived at the crucial point of our approach. From these equations we can formulate a purely initial-value problem as well as a corresponding matrix eigenvalue problem. Applying the finite-difference technique, we undertake this in the following paragraphs.

2.3. Discretization in Space: ODEs in Time

It is well known that the viscoelastic responses of compressible Earth models can be characterized by the exponential-like development in time and by the spatial distribution which could be expressed in terms of the spherical Bessel functions. In other words, the behaviour of the solution $\mathbf{y}(t,r)$ of (58) is considerably different in the directions of each independent variable. For such PDEs a method based on discretization in the spatial dimension, referred to as the method of lines (MOL), represents a powerful solution tool [e.g., *Schiesser,* 1994]. Hereafter we consider only the spheroidal part of PDEs (58), so the solution vector $\mathbf{y}(t,r)$ contains 6 spheroidal elements from now on. Let us consider the staggered grids $\{r_i,\, i = 1,\ldots,J\}$ and $\{x_j,\, j = 0,\ldots,J\}$,

$$b = x_0 < r_1 < x_1 < r_2 < x_2 < \ldots < r_J < x_J = a\,, \tag{71}$$

spreading over the Earth mantle, $b \le r \le a$. In order to express PDEs (58) on the grid $\{r_i\}$ by means of $\mathbf{y}(t,r)$ evaluated on the grid $\{x_j\}$, we employ expansions of $\mathbf{y}(t,r)$ and its first derivative evaluated at r_i by means of weighted sums of $\mathbf{y}_j(t) \equiv \mathbf{y}(t,x_j)$,

$$\mathbf{y}\,(t,r_i) \quad = \quad \textstyle\sum_{j=0}^{J} \alpha_{ij}^{(0)}\mathbf{y}_j(t)\,, \tag{72}$$

$$\mathbf{y}'(t,r_i) \quad = \quad \textstyle\sum_{j=0}^{J} \alpha_{ij}^{(1)}\mathbf{y}_j(t)\,, \tag{73}$$

where $\alpha_{ij}^{(0)}$ and $\alpha_{ij}^{(1)}$ are the weights given by a choice of r_i and x_js. Using (72)–(73) we obtain $6J$ scalar ODEs in time for $6J{+}6$ unknown elements of $\mathbf{y}_j$s by expressing PDEs (58) on the grid $\{r_i\}$,

$$\sum_{j=0}^{J}\left[\alpha_{ij}^{(1)} - \boldsymbol{A}_i\alpha_{ij}^{(0)}\right]\dot{\mathbf{y}}_j(t) \quad = \tag{74}$$

$$= \sum_{j=0}^{J} \left[\xi_i \left(\boldsymbol{D}_i \alpha_{ij}^{(1)} + \boldsymbol{E}_i \alpha_{ij}^{(0)} \right) \right] \mathbf{y}_j(t) , \quad i = 1, \ldots, J ,$$

where $\boldsymbol{A}_i = \boldsymbol{A}_n(r_i)$, $\boldsymbol{D}_i = \boldsymbol{D}_n(r_i)$, $\boldsymbol{E}_i = \boldsymbol{E}_n(r_i)$ and $\xi_i = \xi(r_i)$. The last 6 necessary equations come from spheroidal boundary conditions (65) at $r = a$,

$$\boldsymbol{M}_J \mathbf{y}_J(t) = \sqrt{\frac{4\pi}{2n+1}} \begin{pmatrix} -g_0 \Gamma_n \\ 0 \\ -4\pi G \Gamma_n \end{pmatrix} , \quad (75)$$

$$\boldsymbol{M}_J = \begin{pmatrix} 0 & 0 & 1 & 0 & 0 & 0 \\ 0 & 0 & 0 & 1 & 0 & 0 \\ 0 & 0 & 0 & 0 & 0 & 1 \end{pmatrix} , \quad (76)$$

and the conditions (66) at the centre, $r = b = 0$,

$$\boldsymbol{M}_0 \mathbf{y}_0(t) = 0 , \quad (77)$$

$$\boldsymbol{M}_0 = \begin{pmatrix} 1 & 0 & 0 & 0 & 0 & 0 \\ 0 & 1 & 0 & 0 & 0 & 0 \\ 0 & 0 & 0 & 0 & 1 & 0 \end{pmatrix} , \quad (78)$$

or the conditions (67) at the core-mantle boundary, $r = b > 0$,

$$\boldsymbol{M}_0 \mathbf{y}_0(t) = 0 , \quad (79)$$

$$\boldsymbol{M}_0 = \begin{pmatrix} -\varrho_0^- g_0 & 0 & 1 & 0 & -\varrho_0^- & 0 \\ 0 & 0 & 0 & 1 & 0 & 0 \\ -4\pi G \varrho_0^- & 0 & 0 & 0 & -4\pi G \frac{\varrho_0^-}{g_0} - C & 1 \end{pmatrix} . \quad (80)$$

For the radially discretized solution vector $\mathbf{Y}(t)$ with $6J + 6$ elements,

$$\mathbf{Y}(t) = \left(\mathbf{y}_0(t), \mathbf{y}_1(t), \ldots, \mathbf{y}_J(t) \right)^T , \quad (81)$$

ODEs (74) and the boundary conditions (75) and (77) or (79), differentiated in time, form the resulting system of $6J + 6$ ODEs in time,

$$\boxed{\boldsymbol{P} \dot{\mathbf{Y}}(t) = \boldsymbol{Q} \mathbf{Y}(t) ,} \quad (82)$$

where

$$\boldsymbol{P} = \begin{pmatrix} \boxed{\boldsymbol{M}_0}_{3\times 6} & \boxed{0}_{3\times 6J} \\ \boxed{\alpha_{1j}^{(1)} - \boldsymbol{A}_1 \alpha_{1j}^{(0)}}_{6\times(6J+6)} \\ \vdots \\ \boxed{\alpha_{Jj}^{(1)} - \boldsymbol{A}_J \alpha_{Jj}^{(0)}}_{6\times(6J+6)} \\ \boxed{0}_{3\times 6J} & \boxed{\boldsymbol{M}_J}_{3\times 6} \end{pmatrix} , \quad (83)$$

$$\boldsymbol{Q} \;=\; \begin{pmatrix} \boxed{0}_{3\times(6J+6)} \\ \boxed{\xi_1\left(\boldsymbol{D}_1\alpha_{1j}^{(1)}+\boldsymbol{E}_1\alpha_{1j}^{(0)}\right)}_{6\times(6J+6)} \\ \vdots \\ \boxed{\xi_J\left(\boldsymbol{D}_J\alpha_{Jj}^{(1)}+\boldsymbol{E}_J\alpha_{Jj}^{(0)}\right)}_{6\times(6J+6)} \\ \boxed{0}_{3\times(6J+6)} \end{pmatrix} \tag{84}$$

and $\Gamma_n(t)$ is considered constant in time, i.e., $\dot{\Gamma}_n = 0$. System (82) with the initial condition (69) represents a purely initial-value formulation of the problem of viscoelastic responses of the Earth. For given grids $\{r_i\}$ and $\{x_j\}$, both $\boldsymbol{P}$ and $\boldsymbol{Q}$ are constant matrices. The matrix $\boldsymbol{P}$ is regular for all of the models studied here, so we can write (82) in an equivalent form,

$$\boxed{\dot{\mathbf{Y}}(t) \;=\; \boldsymbol{B}\,\mathbf{Y}(t)\;, \qquad \boldsymbol{B} \;=\; \boldsymbol{P}^{-1}\boldsymbol{Q}\;,} \tag{85}$$

i.e., in the standard form of a linear homogeneous system of ODEs with constant coefficients.

2.4. Modal Decomposition: The Eigenvalue Problem

A solution of ODEs (85), referred to as the fundamental system, can be written [e.g., *Rektorys,* 1994] as a linear combination of the constituents

$$e^{s_p t} \quad \text{or} \quad R_q(t)e^{s_q t}\,, \tag{86}$$

where s_p is any nondegenerate eigenvalue of $\boldsymbol{B}$, s_q any Q-degenerate eigenvalue of $\boldsymbol{B}$ and R_q a polynomial of the maximal degree $Q-1$. Thus, eigenanalysis of matrix $\boldsymbol{B}$ can reveal a substantial information about the behavior of the solution of ODEs (85). It is straightforward to see that a generalized eigenvalue problem,

$$\boldsymbol{Q}\mathbf{Y} \;=\; s\boldsymbol{P}\mathbf{Y}\,, \tag{87}$$

corresponds to ODEs (82), while a standard eigenvalue problem,

$$\boldsymbol{B}\mathbf{Y} \;=\; s\mathbf{Y}\,, \tag{88}$$

matches ODEs (85). In the case of regular matrix $\boldsymbol{P}$ both eigenproblems are formally equivalent. However, there are differences in performance and accuraccy of applicable numerical routines, as will be discussed later.

For a given nondegenerate eigenvalue, $s = s_p$, the corresponding eigenvector $\mathbf{Y}_p$ with $6J+6$ elements gathers the discretized $(J+1)$-eigenvectors U_p, V_p, etc. The response of viscoelastic models to the time impulse, i.e.,

for $f(t) = \delta(t)$, is traditionally expressed by the surface load Love numbers [*Peltier,* 1974],

$$h(t) = h^E\delta(t) + \sum_p r_p^{(h)} \exp(s_p t)\,, \quad (89)$$

$$l(t) = l^E\,\delta(t) + \sum_p r_p^{(l)} \exp(s_p t)\,, \quad (90)$$

$$k(t) = k^E\delta(t) + \sum_p r_p^{(k)} \exp(s_p t)\,, \quad (91)$$

where h^E, l^E and k^E are the elastic load Love numbers and the sums on the right-hand sides describe the non-elastic response. In order to evaluate the non-elastic part of the Love numbers, formulas (8.1)–(8.3) by *Tromp and Mitrovica* [1999] for the partial modal amplitudes can be applied,

$$r_p^{(h)} = \frac{\tau}{2s_p} U_p(g_0 U_p + F_p)\,, \quad (92)$$

$$r_p^{(l)} = \frac{\tau}{2s_p} V_p(g_0 U_p + F_p)\,, \quad \tau = \frac{M}{a}\frac{2n+1}{4\pi}\,, \quad (93)$$

$$r_p^{(k)} = -\frac{\tau}{2g_0 s_p} F_p(g_0 U_p + F_p)\,, \quad (94)$$

where M is the mass of the Earth and the eigenvectors are normalized in accord with the condition (3.6) by *Tromp and Mitrovica* [1999],

$$\int_b^a \frac{\mu\xi}{(s_p+\xi)^2}\left[\frac{1}{3}(2U_p' - F_p)^2 + N X_p^2 + \frac{N(n-1)(n+2)}{r^2} V_p^2\right] r^2\,dr = -2s_p\,. \quad (95)$$

In Fig. 1 we summarize both the Laplacian and eigenvalue approaches and compare the differences in the methodologies between both the secular-determinant and the eigenvalue analysis.

Fig. 1

3. NUMERICAL TECHNIQUES

3.1. Pseudospectral vs. Low-order Finite Differences

A choice of a discretization pattern obviously plays a crucial role for the accuracy of the eigenvalue method. In the derivation of ODEs (82) we have made a rather general choice of the staggered grids $\{r_i\}$ and $\{x_j\}$ in (71). Here we will discuss two particular discretization patterns of this form.

The first discretization pattern is based on high-order pseudospectral (PS) schemes for approximation of zero and first derivatives of a function at an arbitrary point by a weighted sum of known values of the function, cf. (72)–(73),

$$\mathbf{y}\,(t, r_i) = \sum_{j=0}^{J} \alpha_{ij}^{(0)} \mathbf{y}_j(t)\,, \quad (96)$$

$$\mathbf{y}'(t, r_i) = \sum_{j=0}^{J} \alpha_{ij}^{(1)} \mathbf{y}_j(t)\,, \quad (97)$$

where $\mathbf{y}_j(t) \equiv \mathbf{y}(t, x_j)$. The weights $\alpha_{ij}^{(0)}$ and $\alpha_{ij}^{(1)}$, in general non-zero for all i and j, can be computed by the algorithm based on a polynomial approximation [*Fornberg,* 1996]. In order to apply the PS schemes, it is necessary to establish a correspondence between the grids $\{r_i\}$ and $\{x_j\}$ and zeroes and extremas of orthogonal polynomials, respectively; we have made the choice of r_is being the roots of Chebyshev polynomials transformed to $\langle b, a\rangle$ and x_js being the interlaced extremas. For models composed of few layers, we have obtained accurate eigenvalues even with very coarse grids. However, higher grid densities are necessary for realistically stratified models. Then the matrices $\boldsymbol{P}$ and $\boldsymbol{Q}$ become larger and the computational demands of the eigenanalysis of (87), resp. (88) increase quite rapidly.

The other tested discretization pattern is based on low-order finite-difference (FD) schemes. We applied the FD schemes on the equi-spaced staggered grids $\{r_i\}$ and $\{x_j\}$ with $r_i = (x_{i-1} + x_i)/2$ and the constant stepsize $h = r_i - r_{i-1} = x_i - x_{i-1}$. For these grids the following second-order (FD2) and fourth-order (FD4) approximations of $\mathbf{y}(t, r_i)$ and $\mathbf{y}'(t, r_i)$ can be found (e.g., by Fornberg's algorithm),

$$
\begin{aligned}
&\text{FD2} \quad \text{for } i = 1, \ldots, J \\
&\quad \mathbf{y}\,(t, r_i) \;&&= \tfrac{1}{2}\mathbf{y}_{i-1}(t) + \tfrac{1}{2}\mathbf{y}_{i+1}(t)\,, \\
&\quad \mathbf{y}'(t, r_i) \;&&= \left[-\mathbf{y}_{i-1}(t) + \mathbf{y}_{i+1}(t)\right]/h\,, \\
&\text{FD4} \quad \text{for } i = 1 \\
&\quad \mathbf{y}\,(t, r_1) \;&&= \tfrac{5}{16}\mathbf{y}_0 + \tfrac{15}{16}\mathbf{y}_1 - \tfrac{5}{16}\mathbf{y}_2 + \tfrac{1}{16}\mathbf{y}_3\,, \\
&\quad \mathbf{y}'(t, r_1) \;&&= \left[-\tfrac{23}{24}\mathbf{y}_0(t) + \tfrac{7}{8}\mathbf{y}_1(t)\right. \\
&\qquad\qquad &&+ \left.\tfrac{1}{8}\mathbf{y}_2(t) - \tfrac{1}{24}\mathbf{y}_3(t)\right]/h\,, \\
&\text{FD4} \quad \text{for } i = 2, \ldots, J-1 \\
&\quad \mathbf{y}\,(t, r_i) \;&&= -\tfrac{1}{16}\mathbf{y}_{i-2} + \tfrac{9}{16}\mathbf{y}_{i-1} + \tfrac{9}{16}\mathbf{y}_{i+1} - \tfrac{1}{16}\mathbf{y}_{i+2}\,, \\
&\quad \mathbf{y}'(t, r_i) \;&&= \left[\tfrac{1}{24}\mathbf{y}_{i-2}(t) - \tfrac{9}{8}\mathbf{y}_{i-1}(t)\right. \\
&\qquad\qquad &&+ \left.\tfrac{9}{8}\mathbf{y}_{i+1}(t) - \tfrac{1}{24}\mathbf{y}_{i+2}(t)\right]/h\,, \\
&\text{FD4} \quad \text{for } i = J \\
&\quad \mathbf{y}\,(t, r_J) \;&&= \tfrac{1}{16}\mathbf{y}_{J-3} - \tfrac{5}{16}\mathbf{y}_{J-2} + \tfrac{15}{16}\mathbf{y}_{J-1} + \tfrac{5}{16}\mathbf{y}_J\,, \\
&\quad \mathbf{y}'(t, r_J) \;&&= \left[\tfrac{1}{24}\mathbf{y}_{J-3}(t) - \tfrac{1}{8}\mathbf{y}_{J-2}(t)\right. \\
&\qquad\qquad &&- \left.\tfrac{7}{8}\mathbf{y}_{J-1}(t) + \tfrac{23}{24}\mathbf{y}_J(t)\right]/h\,.
\end{aligned}
$$

Although it is easier to implement, the eigenanalysis based on the low-order FD schemes is inferior to the high-order PS schemes in terms of accuracy.

We have also tested the case of overlapping grids $\{r_i\}$ and $\{x_j\}$. The results have been less satisfactory than those obtained on the staggered grids since more discretization modes contaminated the physical part of eigenspectra. Other patterns of discretization can sure-

ly be designed, for instance that motivated by the fact that three elements of $\mathbf{y}(t,r)$ correspond to the first derivatives of the other three. In the future we will surely find the most optimal discretization stencil for the purpose of determining the eigenvalues.

3.2. Eigenpackages

In (87) and (88) we have obtained both the generalized and standard eigenvalue problems, respectively. The $(6J+6)\times(6J+6)$ matrices $\boldsymbol{P}$ and $\boldsymbol{Q}$ of the generalized problem are both non-symmetric. While for the PS schemes the matrices are full, they become band diagonal for the FD schemes. There are 8 sub- and 8 superdiagonals for the FD2 scheme and 20 sub- and 20 superdiagonals for the FD4 scheme, as can be deduced from (83)–(84) and (59)–(61). The $(6J+6)\times(6J+6)$ matrix $\boldsymbol{B}$ of the standard problem is non-symmetric and full for all tested schemes. However, a number of CPU operations needed to evaluate $\boldsymbol{B}$ grows with J^3 for PS schemes and only with J for FD schemes. We note that the real-space FD method with up to 12th-order accuracy has been employed to solve eigenvalue problems in solid-state physics for complex systems with thousands of atoms [*Stathopoulos et al.,* 2000].

A synopsis of the available numerical methods, including both direct and iterative techniques for large-scale eigenvalues, can be found in the book by *Trefethen and Bau* [1997]. Standard numerical libraries (e.g., LAPACK, NAG, IMSL) contain several routines for matrix eigenanalysis. The routines usually perform the following tasks for both standard and generalized problems: (EV) evaluation of all eigenvalues and no eigenvectors, (EVV) evaluation of all eigenvalues and all eigenvectors, (EsV) evaluation of all eigenvalues in a selected interval, (EI) evaluation of an eigenvector to a known eigenvalue. The task (EV) is generally solved by a two-step algorithm based on the reduction to Hessenberg form and the QR algorithm. A similar algorithm is used for the task (EVV). For tasks performing selections, (EsV) and (EI), an algorithm based on inverse iteration is usually invoked. An extensive package of eigenroutines can be found in both LAPACK and NAG, which contain routines for all tasks mentioned above. In both these libraries there are also routines available for the task (EI) and the generalized problem with band diagonal matrices. IMSL contains routines for the tasks (EV) and (EVV).

We have tested routines for both the standard and generalized eigenproblems (87)–(88). In both cases the total CPU-times were comparable but the accuracy of the solvers of standard eigenproblems was substantial-

ly better. The maximal grid density we employed was for $J \approx 300$ with the approximate matrix dimensions of $1,800 \times 1,800$. It is a number of operations which seems to be the main obstacle for higher resolution, as it grows with J^3 (see Table 1), while the memory requirement grows with J^2. Large-scale eigenvalue problems involving pseudospectra are now becoming more common in all fields of science and engineering [e.g., *Trefethen,* 1999]. For solving the eigenproblems with large matrices (say, up to $10^6 \times 10^6$), other family of methods, based on the Krylov subspace methods, has to be invoked [*Saad,* 1992]. A package, reffered to as the implicitly-restarted Arnoldi method, is implemented in ARPACK [*Lehoucq et al.,* 1998], a publicly available library for solving large eigenvalue problems.

Table 1

4. APPLICATIONS

We first demonstrate the numerical ability of the eigenvalue method to catch the eigenspectra of the homogeneous spheres ($a = 6,371$ km, $\varrho_0 = 5,517$ kg m^{-3}, $\mu = 1.4519 \times 10^{11}$ Pa, $\eta = 10^{21}$ Pa s), both incompressible (λ infinite) and compressible ($\lambda = 3.5288 \times 10^{11}$ Pa). The calculations were carried out for selected angular orders up to the degree 120 and using the PS discretization [*Fornberg,* 1996] on the Chebyshev grids of 30, 60 and 120 layers. The eigenspectrum of the homogeneous incompressible sphere is shown in Fig. 2a. There is only one branch of the physical relaxation modes, denoted by M0, the well-known mantle modes, which can be obtained analytically [*Wu and Peltier,* 1982]. We reached the accuracy with more than 10 digits for all tested grid densities. As the analyzed matrices are non-symmetric, their eigenvalues can, in general, be complex. However, all the M0 eigenvalues are real and nondegenerate and thus they yield the classical exponential relaxation.

Fig. 2

The branch of eigenvalues denoted by s_M lies in the position of $s = -\mu/\eta$, i.e., of the inverse Maxwell time. These eigenvalues are $3J$-degenerate, so they could yield degenerate normal modes (cf. s_q in (86)). In the Laplacian spectral analysis, they are considered to represent false singularities, which should be removed [*Wu and Ni,* 1996; *Boschi et al.,* 1999]. *Hanyk et al.* [1999] showed numerically by direct integration in the time domain that no significant deformation energy is associated with other than the M0 mode.

The branch denoted by X consists of real positive nondegenerate eigenvalues. Unlike the branches M0 and s_M, the branch X is strongly grid-sensitive. The tendency of shifting the eigenvalues towards zero is exhibited with increasing number of grid points, which is demonstrated for the grid densities of 30, 60 and 120 layers

and which can serve for identification of these modes. As the X-eigenvalues are obviously caused by the radial discretization of the model, we refer to the corresponding modes as the discretization modes. There is also a band of eigenvalues in the region of small s, several orders of magnitude apart from the physical eigenvalues. This is the "numerical noise" produced by the iterative eigenroutines, different for different eigenroutines, grid densities and discretization schemes.

The eigenspectrum of the homogeneous compressible sphere is presented in Fig. 2b for the PS discretization on the Chebyshev grid of 30 layers. In comparison with the spectrum of the incompressible sphere, there are two more groups of modal branches, associated with compressibility. The first group consists of the dilatation or D-modes [*Vermeersen et al.,* 1996], whereas the second group is formed by the Rayleigh-Taylor (RT) modes, generated by the subadiabatic gradient of density [*Hanyk et al.,* 1999]. There are about J D-modes and J RT-modes. The (negative) D-eigenvalues $s^{(i)}$ can be indexed such that $\mathrm{Re}\, s^{(i)} < \mathrm{Re}\, s^{(i+1)}$. About a half of the computed D-eigenvalues is purely real and corresponds to the analytically derived values [*Hanyk et al.,* 1999] with a high accuracy. Since the corresponding eigenvectors are of oscillatory character with the number of oscillations increasing with increasing i, see Fig. 3, the resolution of the grid is not sufficient for higher i and those D-eigenvalues become corrupted (they are complex and the real parts do not fit the analytical values). Similarly, this is also true for the RT modes. We emphasize that all the RT-eigenvalues are positive (or have positive real parts) and describe thus the onset of exponential collapse of the studied system. We also point out that the Maxwell eigenvalues are $2J$-degenerate in this case, that the X-eigenvalues obtained on the equivalent grids are almost identical for both incompressible and compressible spheres and that the low-s spectral region for the compressible sphere is again contaminated by the numerical noise.

Fig. 3

The sensitivity of the discretization modes to applied discretization schemes is shown in Fig. 4, where we deal with the core-mantle-lithosphere incompressible model with the following choice of the parameters: $a = 6,371$ km, $b = 3,480$ km, $\varrho_0 = 4,314$ kg m^{-3}, $\mu = 1.4519 \times 10^{11}$ Pa and $\eta = 10^{21}$ Pa s in the mantle, $\varrho_0 = 10,926$ kg m^{-3} in the core and the depth of the lithosphere equal to 120 km. We have studied the eigenspectra of this model for the two different discretizations: a) 20 grid layers in the mantle and 10 grid layers in the lithosphere with the PS scheme employed over the Chebyshev nodal points spread separately in each

Fig. 4

of the layers, b) 20 layers of equal thickness in the mantle and 10 layers of equal thickness in the lithosphere with the FD2 scheme employed. One can clearly recognize the branches of the modes M0, L0 and C0 as well as the branch of the Maxwell eigenvalues, all insensitive to discretization. On the other hand, the spectral branches of the discretization modes are completely different for the PS and the FD2 scheme. While the discretization spectrum consists from one branch of stable modes and one branch of unstable modes in the former case, there exist several branches of modes, both stable and unstable, in the latter case. However, the growth time of the first unstable discretization mode produced by the FD2 scheme is by an order of magnitude higher than that of the first unstable X-mode by the PS scheme.

In Fig. 5 we present the eigenspectra for other six simple incompressible models, which were already studied by *Wu and Peltier* [1982]. Model A is the homogeneous sphere discussed above, B has the 120-km thick elastic lithosphere, C has the mantle density 4,314 $\mathrm{kg\,m^{-3}}$ and an inviscid core of radius 3,485.5 km and the density 10,926 $\mathrm{kg\,m^{-3}}$, D has an outer shell of thickness 195.6 km in which the density is reduced from 5,600 $\mathrm{kg\,m^{-3}}$ to 3,200 $\mathrm{kg\,m^{-3}}$ and the shear modulus from 1.4519×10^{11} Pa s to 0.7260×10^{11} Pa s, E (F) differ from A by a two-order increase (decrease) of viscosity below (above) the depth of 671 (120) km. The eigenspectra are evaluated by the low-order FD2 discretization with 60 layers employed in each case. We obtained the modal branches visually equivalent with those published by *Wu and Peltier* [1982] in their Fig. 2. There are also groups of the degenerate Maxwell eigenvalues in our eigenspectra. The discretization modes are out of the extent of the panels for the chosen grid densities.

Fig. 5

In the eigenvalue method we have a fast, easy and complete tool for finding modes of realistic compressible models with arbitrary radial variations of the density and rheology parameters. The eigenvalues of such a model are shown in Fig. 6. The density and the elastic parameters are taken from the PREM, the elastic lithosphere of 120-km thickness is considered and the viscosity of the upper (lower) mantle is set to 10^{21} (2×10^{21}) Pa s. *Tromp and Mitrovica* [1999] presented a subset of eigenvalues for this model in their Fig. 1. However, there are lots of other modes (D-modes, RT-modes). Here we point out to the RT modes with all the growth times higher than 100 Myr. The physical reason, why these characteristic times of the model instability are much longer in comparison with the homogeneous sphere, is that the PREM is effectively subadiabatic on-

Fig. 6

ly in the upper mantle above the transition zone. The question whether the mantle can be subadiabatic also in other regions is not satisfactorily resolved but thermal convection models point to the possibility that the lower mantle above the D" layer could also be subadiabatic [*Matyska and Yuen,* 2000], which may result in global instabilities over shorter timescales. There is also a band of the dilatation modes and degenerate Maxwell eigenvalues corresponding to relaxation times between 100 and 1000 years. This band is substantially broadened if a model with variable viscosity is used. In Fig. 7 we present the eigenspectrum of another PREM-based model with a high-viscosity hill in the lower mantle [*Ricard and Wuming,* 1991; *Forte and Mitrovica,* 2001] and a low-viscosity zone in the upper mantle (viscous profile C2 by *Hanyk et al.* [1996]). The bandwidth of the rectangular region formed by the dilatation modes and the Maxwell eigenvalues spans over four orders of magnitude. One can discern that the M0 and L0 branches of the physical modes are buried inside this region. It is like to find needles in a haystack, if one tries to locate these "true" modes by means of the classical root-finding methods.

Fig. 7

5. CONCLUDING REMARKS

In this paper we have demonstrated the feasibility of using eigenvalue analysis for determining the relaxation times for both incompressible and compressible self-gravitating stratified viscoelastic Earth models. Such an approach yields the full spectrum of both the relaxation and growth times of a model after discretization, its implementation is easy and computational cost is low. The crucial idea was to recast the governing equations into a mixed set of PDEs (58), and then to apply the method of lines for obtaining the set of ODEs (82) in time. Our previous approach [*Hanyk et al.,* 1995; 1996; 1998] consists in first integration over time and then solving a two-point boundary value problem in the radius, i.e., we applied the Rothe method [*Rektorys,* 1982]. However, the Rothe method does not allow one to carry out an eigenanalysis of the temporal relaxations. In this regard, we note that the resultant set of ODEs (82) can also be solved by direct time-integration. In other words, the set of ODEs (82) can be employed for a different initial-value approach, where stiff time-integrators can substantially reduce the number of timesteps. Our approach can be adopted for anelastic rheologies, such as the standard linear solid which may be important for lithospheric bending [*Schmalholz and Podladchikov,* 2001]. The understanding of the tectonic impact of the potential energy change and geoid anomalies caused by

earthquakes along plate margins can be investigated using the eigenfunctions generated with short time-scale rheology. Computationally this approach can be very fast for summing up cumulatively the gravitational excitation from many large earthquakes [*Tanimoto and Okamoto,* 2001]. This eigenvalue approach can also be useful in understanding crustal instabilities involving folding of lithospheric rocks [*Schmalholz and Podladchikov,* 1999; 2001].

Acknowledgments. We wish to thank Yu. Podladchikov and S. Schmalholz for inspiring discussions, L. Boschi for a careful review and L. L. A. Vermeersen for useful editorial comments. This research has been supported by the Research Project MŠMT J13/98: 113200004, the Grant Agency of the Czech Republic under Nos. 205/00/0906 and 205/00/D113, the Charles University grants 170/1998/B-GEO/MFF and 175/2000/B-GEO/MFF, the geoscience program of the D.O.E. and the geophysics program of the National Science Foundation.

REFERENCES

Ascher, U. M., and L. R. Petzold, *Computer Methods for Ordinary Differential Equations and Differential-Algebraic Equations,* SIAM, Philadephia, 1998.

Backus, G. E., Converting vector and tensor equations to scalar equations in spherical coordinates, *Geophys. J. R. astr. Soc., 13,* 71–101, 1967.

Boschi, L., J. Tromp, and R. J. O'Connell, On Maxwell singularities in postglacial rebound, *Geophys. J. Int., 136,* 492–498, 1999.

Christensen, R. M., *Theory of Viscoelasticity: An Introduction,* Academic, New York, 1982.

Dahlen, F. A., and J. Tromp, *Theoretical Global Seismology,* Princeton University Press, Princeton, New Jersey, 1998.

Dziewonski, A. M., and D. L. Anderson, Preliminary reference Earth model, *Phys. Earth Planet. Int., 25,* 297–356, 1981.

Fang, M., Static deformation of the outer core, in *Dynamics of the Ice Age Earth: A Modern Perspective,* edited by P. Wu, pp. 155–190, Trans. Tech Publ., Zürich, Switzerland, 1998.

Fang, M., and B. H. Hager, The singularity mystery associated with a radially continuous Maxwell viscoelastic structure, *Geophys. J. Int., 123,* 849–865, 1995.

Farrell, W. E., Deformation of the earth by surface loads, *Rev. Geophys. Space Phys., 10,* 761–797, 1972.

Fornberg, B., *A Practical Guide to Pseudospectral Methods,* Cambridge, New York, 1996.

Forte, A. M., and J. X. Mitrovica, Deep-mantle high-viscosity flow and thermochemical stucture inferred from seismic and geodynamic data, *Nature, 410,* 1049–1056, 2001.

Han, D., and J. Wahr, The viscoelastic relaxation of a realistically stratified earth, and a further analysis of postglacial rebound, *Geophys. J. Int., 120,* 287–311, 1995.

Hanyk, L., C. Matyska, and D. A. Yuen, Initial-value approach for viscoelastic responses of the Earth's mantle, in *Dynamics of the Ice Age Earth: A Modern Perspective,* edited by P. Wu, pp. 135–154, Trans. Tech Publ., Zürich,

Switzerland, 1998.

Hanyk, L., C. Matyska, and D. A. Yuen, Secular gravitational instability of a compressible viscoelastic sphere, *Geophys. Res. Lett., 26,* 557–560, 1999.

Hanyk, L., Matyska, C. and Yuen, D.A., The problem of viscoelastic relaxation of the Earth solved by a matrix eigenvalue approach based on discretization in grid space, *Electronic Geosciences, 5,* http://link.springer.de/link/service /journals/10069/discussion/evmol/evmol.htm, 2000.

Hanyk, L., J. Moser, D. A. Yuen, and C. Matyska, Time-domain approach for the transient responses in stratified viscoelastic Earth models, *Geophys. Res. Lett., 22,* 1285–1288, 1995.

Hanyk, L., D. A. Yuen, and C. Matyska, Initial-value and modal approaches for transient viscoelastic responses with complex viscosity profiles, *Geophys. J. Int., 127,* 348–362, 1996.

Karato, S.-I., Micro-physics of post glacial rebound, in *Dynamics of the Ice Age Earth: A Modern Perspective,* edited by P. Wu, pp. 351–364, Trans. Tech Publ., Zürich, Switzerland, 1998.

Lehoucq, R. B., D. C. Sorensen, and C. Yang, *ARPACK User's Guide: Solution of Large-Scale Eigenvalue Problems with Implicitly Restarted Arnoldi Methods,* SIAM, Philadelphia, 1998.

Martinec, Z., Spectral, initial value approach for viscoelastic relaxation of a spherical earth with a three-dimensional viscosity – I. Theory, *Geophys. J. Int., 137,* 469–488, 1999.

Matyska, C., and D. A. Yuen, Profiles of the Bullen parameter from mantle convection modelling, *Earth Planet. Sci. Lett., 178,* 39–46, 2000.

Nakada, M., Implications of a non-adiabatic density gradient for the Earth's viscoelastic response to surface loading, *Geophys. J. Int., 137,* 663–674, 1999.

Peltier, W. R., The impulse response of a Maxwell earth, *Rev. Geophys. Space Phys., 12,* 649–669, 1974.

Plag, H.-P., and H.-U. Jüttner, Rayleigh-Taylor instabilities of a self-gravitating Earth, *J. Geodynamics, 20,* 267–288, 1995.

Rektorys, K., *The Method of Discretization in Time and Partial Differential Equations,* Reidel, Dordrecht-Boston-London, 1982.

Rektorys, K., *Survey of Applicable Mathematics,* Kluwer, Dordrecht, 1994.

Ricard, Y., and B. Wuming, Inferring the viscosity and the 3-D density structure of the mantle from geoid, topography and plate tectonics, *Geophys. J. Int., 105,* 561–571, 1991.

Saad, Y., *Numerical Methods for Large Eigenvalue Problems,* Manchester University Press, Manchester, England, 1992.

Schiesser, W. E., *Computational Mathematics in Engineering and Applied Science: ODEs, DAEs, and PDEs,* CRC, Florida, 1994.

Schmalholz, S. M., and Yu. Podladchikov, Buckling versus folding: Importance of viscoelasticity, *Geophys. Res. Lett., 26,* 2641–2644, 1999.

Schmalholz, S. M., and Y. Y. Podladchikov, Viscoelastic folding: Maxwell versus Kelvin rheology, *Geophys. Res. Lett., 28,* 1835–1838, 2001.

Spada, G., R. Sabadini, D. A. Yuen, and Y. Ricard, Effects on post-glacial rebound from the hard rheology in the

transition zone, *Geophys. J. Int., 109,* 683–700, 1992.
Stathopoulos, A., S. Ogut, Y. Saad, J. Chelikowsky, and H. Kim, Parallel methods and tools for predicting material properties, *Computing in Science and Engineering, 2,* 19–32, 2000.
Tanimoto, T., and T. Okamoto, Tectonic significance of potential energy change by earthquakes, *J. Geophys. Res.,* in press, 2001.
Trefethen, L. N., *Computation of pseudospectra,* Acta Numerica, Vol. 8, 247–295, Cambridge University Press, 1999.
Trefethen, L. N., and D. Bau, *III. Numerical Linear Algebra,* SIAM, Philadelphia, 1997.
Tromp, J., and J. X. Mitrovica, Surface loading of a viscoelastic earth–II. Spherical models, *Geophys. J. Int., 137,* 856–872, 1999.
Tromp, J., and J. X. Mitrovica, Surface loading of a viscoelastic planet–III. Aspherical models, *Geophys. J. Int., 140,* 425–441, 2000.
Vermeersen, L. L. A., and J. X. Mitrovica, Gravitational stability of spherical self-gravitating relaxation models, *Geophys. J. Int., 142,* 351–360, 2000.
Vermeersen, L. L. A., R. Sabadini, and G. Spada, Compressible rotational deformation, *Geophys. J. Int., 126,* 735–761, 1996.
Wolf, D., Gravitational viscoelastodynamics for a hydrostatic planet, Habilitation Thesis, Bayerische Akademie der Wissenschaften, München, Germany, 1997.
Wu, P., and Z. Ni, Some analytical solutions for the viscoelastic gravitational relaxation of a two-layer non-self-gravitating incompressible spherical earth, *Geophys. J. Int., 126,* 413–436, 1996.
Wu, P., and W. R. Peltier, Viscous gravitational relaxation, *Geophys. J. R. astr. Soc., 70,* 435–485, 1982.
Yuen, D. A., and W. R. Peltier, Normal modes of the viscoelastic earth, *Geophys. J. R. astr. Soc., 69,* 495–526, 1982.

L. Hanyk and C. Matyska, Department of Geophysics, Faculty of Mathematics and Physics, Charles University, V Holešovičkách 2, 18000 Praha, Czech Republic. (e-mail: ladislav.hanyk@mff.cuni.cz; ctirad.matyska@mff.cuni.cz)

D. A. Yuen, University of Minnesota Supercomputing Institute, 1200 Washington Avenue South, Minneapolis, MN 55415. (e-mail: davey@krissy.msi.umn.edu)

Fig. 1

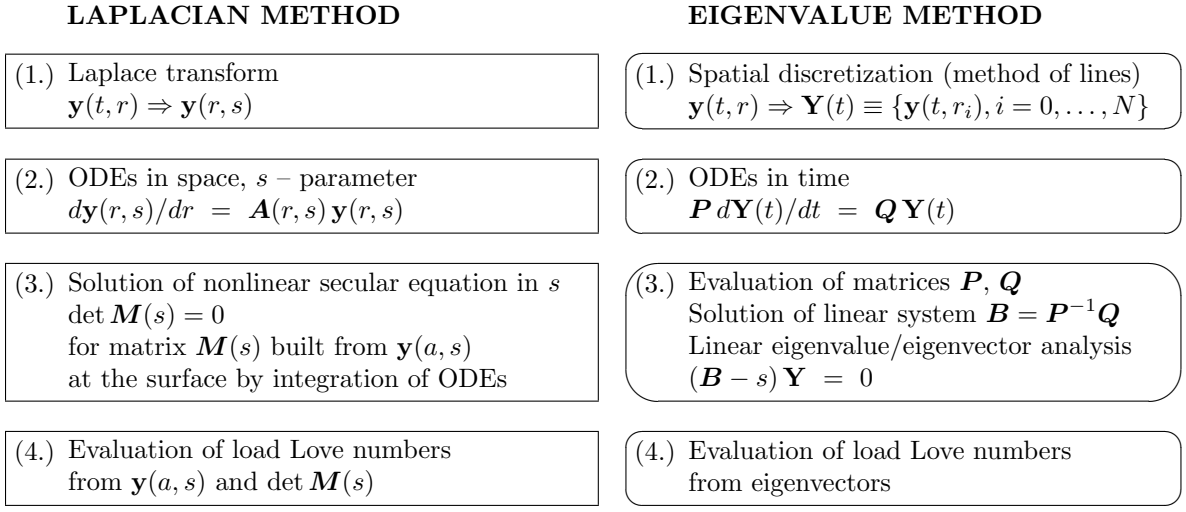

Figure 1. A comparison of the respective sequential steps to be followed in the Laplacian transform method (frames on the left) and the eigenvalue method based on the method of lines (frames on the right) for evaluation of relaxation times and load Love numbers describing the viscoelastic responses to a surface load.

Figure 1. A comparison of the respective sequential steps to be followed in the Laplacian transform method (frames on the left) and the eigenvalue method based on the method of lines (frames on the right) for evaluation of relaxation times and load Love numbers describing the viscoelastic responses to a surface load.

Fig. 2

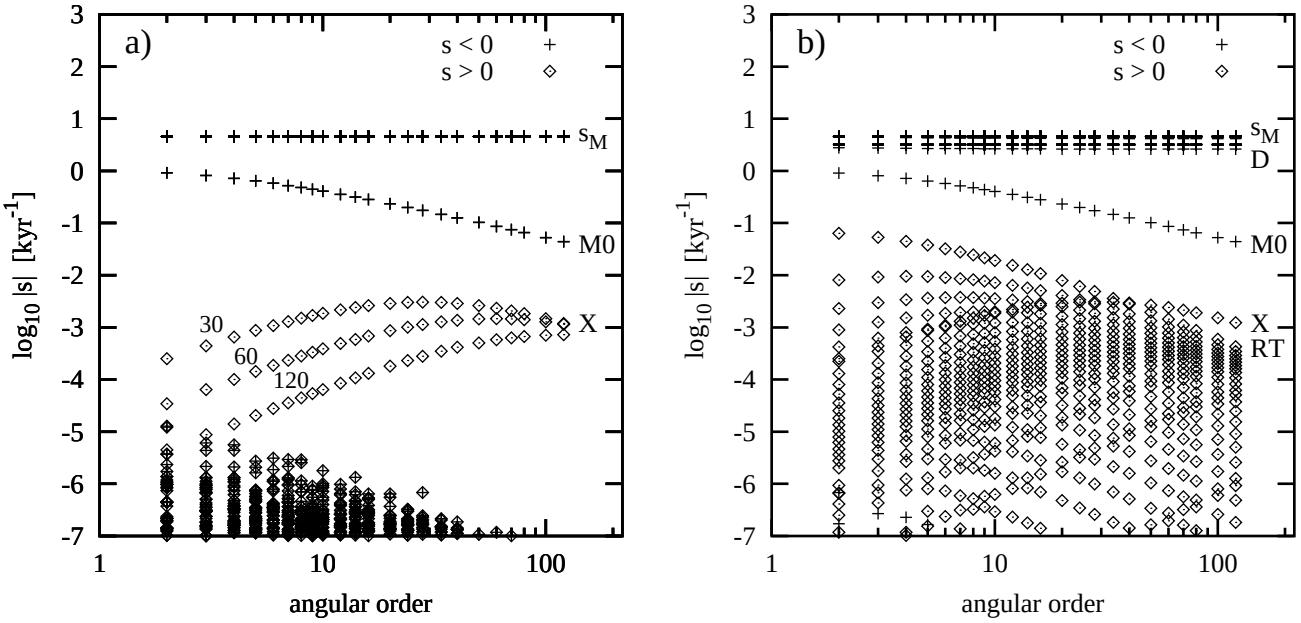

Figure 2. Eigenspectra of the incompressible (panel a) and the compressible (panel b) homogeneous spheres. Both stable and unstable modal branches are plotted (symbols + and ◇ used for negative and positive eigenvalues, respectively). Branches from top to bottom, panel a: Maxwell eigenvalues (s_M), M0 modes, unstable discretization modes (X), panel b: Maxwell eigenvalues, dilatation modes (D), M0 modes and unstable Rayleigh-Taylor modes (RT) crossed by a branch of discretization modes (X). The pseudospectral discretization schemes on the Chebyshev grids have been invoked. The shift of the X-modes towards to longer growth times is demonstrated by presenting the X-branches for the three grid densities (30, 60 and 120 layers) in panel a; the only grid of 30 layers has been used for panel b. The region of $s < 10^{-5}$ kyr^{-1} is contaminated by spurious eigenvalues which result from the iterative character of the applied eigenroutine.

Figure 2. Eigenspectra of the incompressible (panel a) and the compressible (panel b) homogeneous spheres. Both stable and unstable modal branches are plotted (symbols + and ◇ used for negative and positive eigenvalues, respectively). Branches from top to bottom, panel a: Maxwell eigenvalues (s_M), M0 modes, unstable discretization modes (X), panel b: Maxwell eigenvalues, dilatation modes (D), M0 modes and unstable Rayleigh-Taylor modes (RT) crossed by a branch of discretization modes (X). The pseudospectral discretization schemes on the Chebyshev grids have been invoked. The shift of the X-modes towards to longer growth times is demonstrated by presenting the X-branches for the three grid densities (30, 60 and 120 layers) in panel a; the only grid of 30 layers has been used for panel b. The region of $s < 10^{-5}$ kyr^{-1} is contaminated by spurious eigenvalues which result from the iterative character of the applied eigenroutine.

Fig. 3

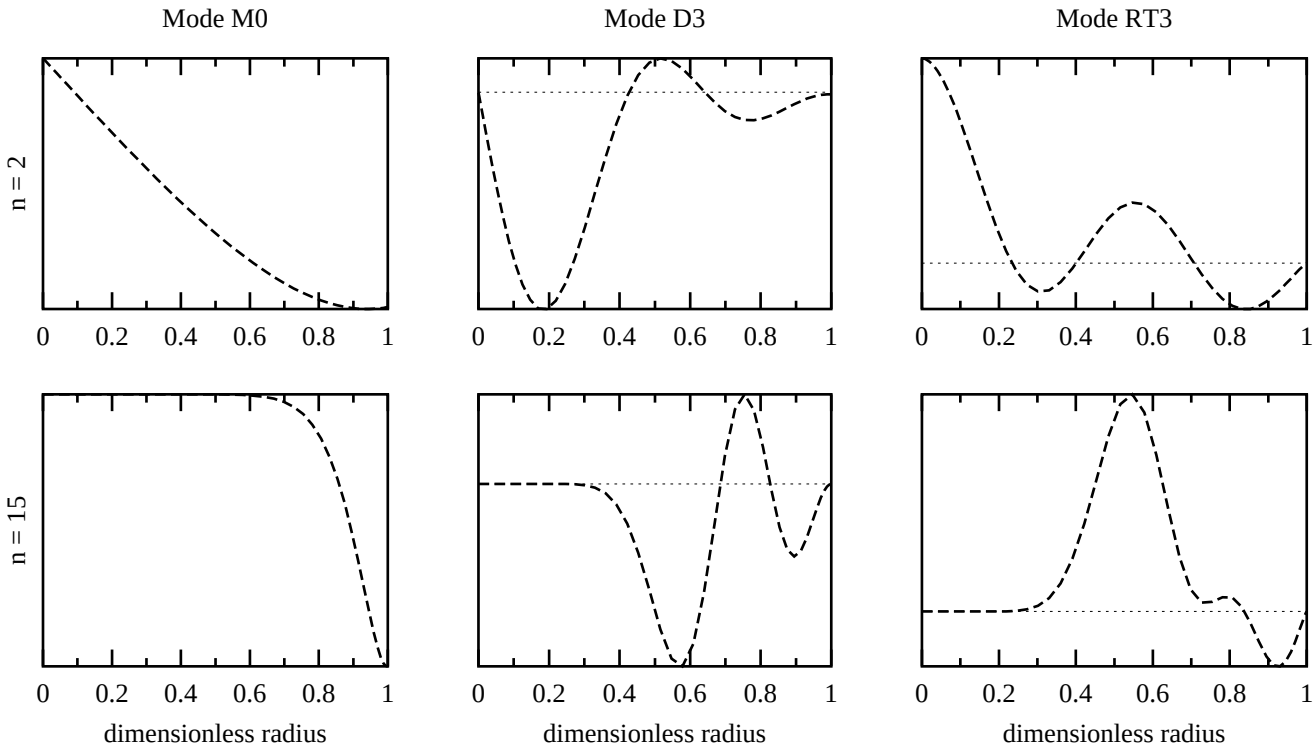

Figure 3. Vertical-displacement eigenvectors U_2 and U_{15} of the homogeneous compressible sphere corresponding to the M0, D3 and RT3 modes computed on the grid of 120 layers using the PS discretization scheme. The vertical bounds correspond with the extremas of the presented eigenvectors. The horizontal zerolines are marked with the dotted lines.

Figure 3. Vertical-displacement eigenvectors U_2 and U_{15} of the homogeneous compressible sphere corresponding to the M0, D3 and RT3 modes computed on the grid of 120 layers using the PS discretization scheme. The vertical bounds correspond with the extremas of the presented eigenvectors. The horizontal zerolines are marked with the dotted lines.

Fig. 4

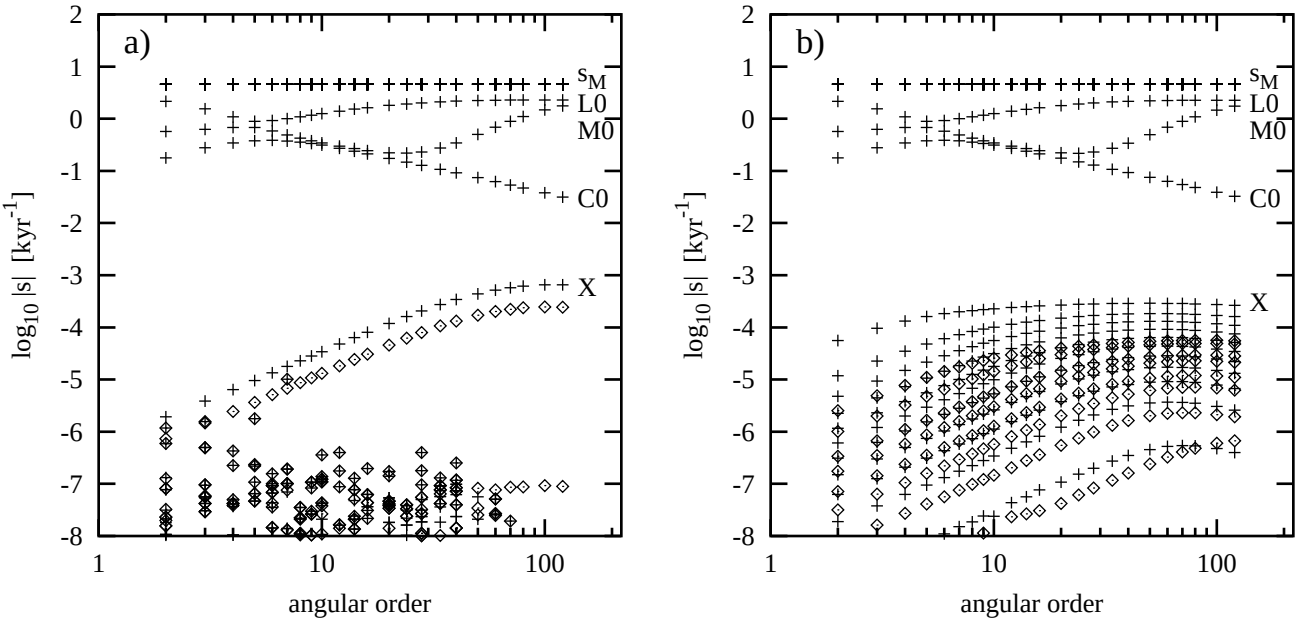

Figure 4. The eigenspectrum of the core-mantle-lithosphere incompressible model evaluated by the PS (panel a) and FD2 (panel b) discretization schemes. The grids of 30 layers (20 in the mantle, 10 in the lithosphere) have been employed in both cases. Besides the classical relaxation modes M0, L0 and C0, there is a branch of the Maxwell eigenvalues (s_M) and the branches of the discretization modes; those with the greatest $|s|$ have been labelled by X. Symbols + and ◇ have been used in the same manner as in Fig. 2.

Figure 4. The eigenspectrum of the core-mantle-lithosphere incompressible model evaluated by the PS (panel a) and FD2 (panel b) discretization schemes. The grids of 30 layers (20 in the mantle, 10 in the lithosphere) have been employed in both cases. Besides the classical relaxation modes M0, L0 and C0, there is a branch of the Maxwell eigenvalues (s_M) and the branches of the discretization modes; those with the greatest $|s|$ have been labelled by X. Symbols + and ◇ have been used in the same manner as in Fig. 2.

Fig. 5

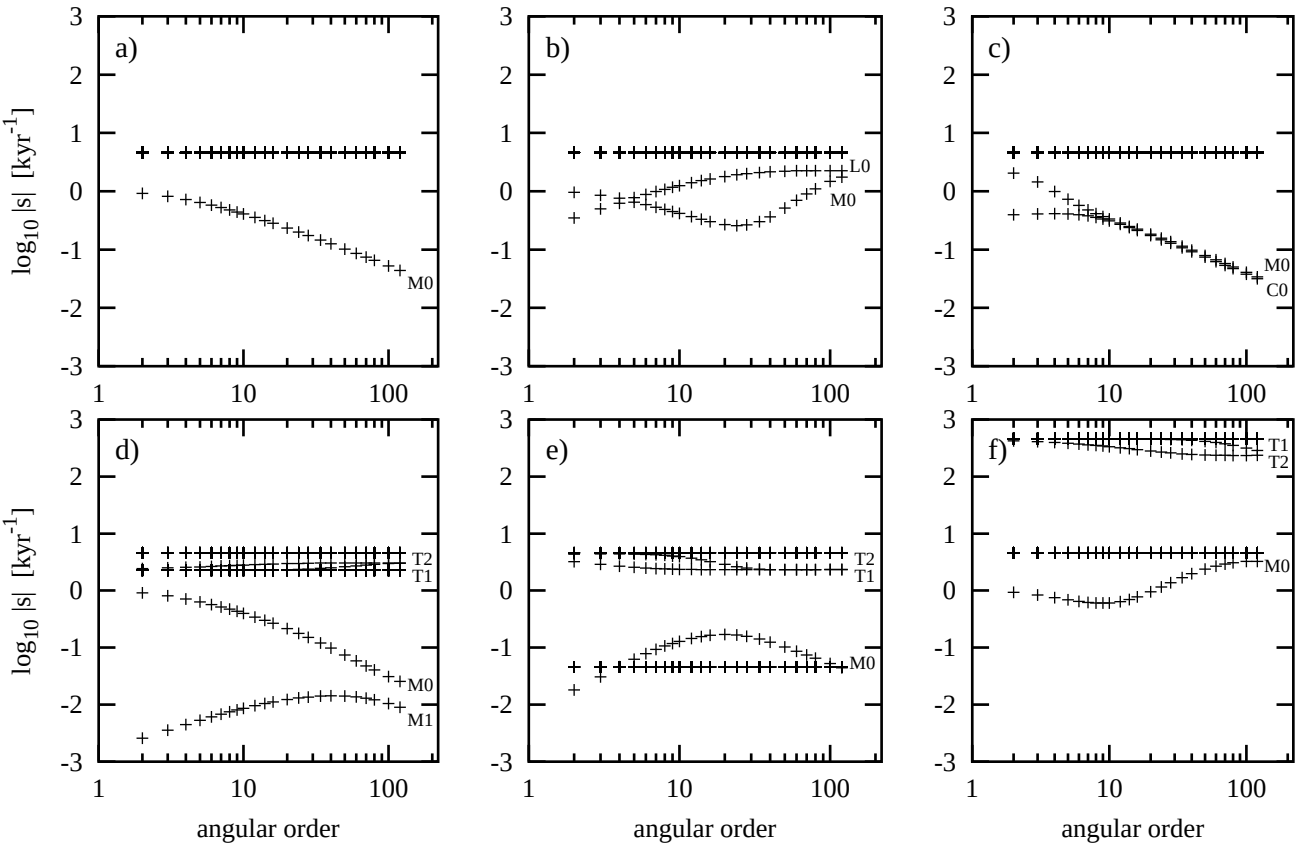

Figure 5. Eigenspectra of the six incompressible models described in the text. The FD2 scheme and equi-spaced grids of 60 layers (for models with two shells: 40 in the lower shell, 20 in the upper shell) have been employed. The extent of the axes and the labelling of the modes has been chosen similarly as in Fig. 2 by *Wu and Peltier* [1982], symbols + and ◇ have been used similarly as in Fig. 2 above.

Figure 5. Eigenspectra of the six incompressible models described in the text. The FD2 scheme and equi-spaced grids of 60 layers (for models with two shells: 40 in the lower shell, 20 in the upper shell) have been employed. The extent of the axes and the labelling of the modes has been chosen similarly as in Fig. 2 by *Wu and Peltier* [1982], symbols + and ◇ have been used similarly as in Fig. 2 above.

Fig. 6

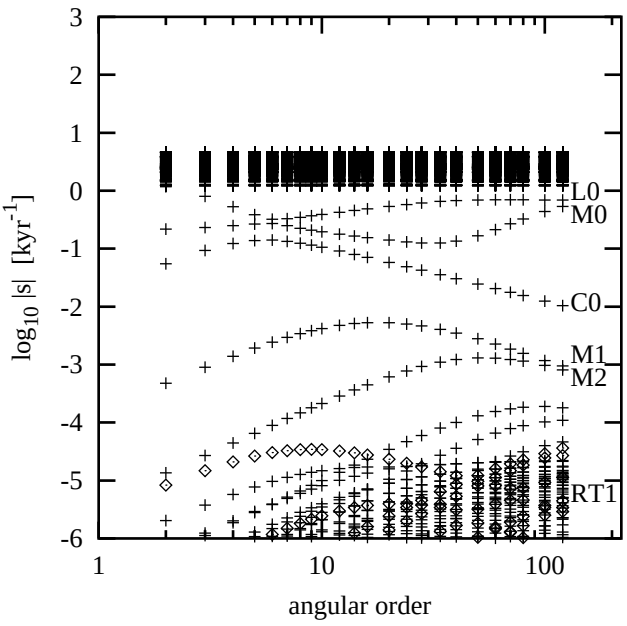

Figure 6. The eigenspectrum of the realistic Earth model (PREM for the density and elastic parameters) with the viscosity of the upper (lower) mantle set to 10^{21} (2×10^{21}) Pa s, discretized on the grid of 240 layers. The classical relaxation modes (M0, L0, C0, M1 and M2) have been labelled as well as the first branch of the unstable RT modes (symbols $\diamond$) on the time scale of 10^5 kyr. There is a lot of discretization X-modes, as the FD2 scheme has been employed (cf. Fig. 4b).

Figure 6. The eigenspectrum of the realistic Earth model (PREM for the density and elastic parameters) with the viscosity of the upper (lower) mantle set to 10^{21} (2×10^{21}) Pa s, discretized on the grid of 240 layers. The classical relaxation modes (M0, L0, C0, M1 and M2) have been labelled as well as the first branch of the unstable RT modes (symbols $\diamond$) on the time scale of 10^5 kyr. There is a lot of discretization X-modes, as the FD2 scheme has been employed (cf. Fig. 4b).

Fig. 7

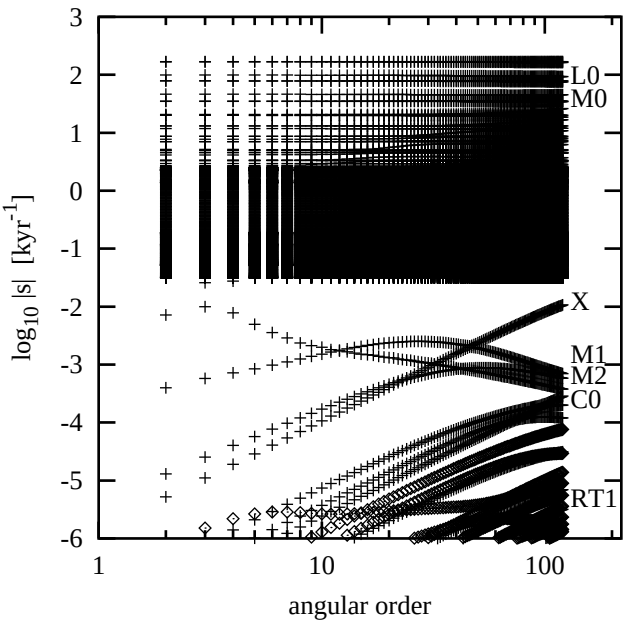

Figure 7. The eigenspectrum of the realistic Earth model (PREM for the density and elastic parameters) with the continuously changing viscous profile in the range from 10^{19} Pa s in the asthenosphere up to more than 10^{23} Pa s in the mid lower mantle, discretized on the grid of 300 Chebyshev layers. The PS scheme has been employed. The classical relaxation modes (M0, L0, C0, M1 and M2) are present but occasionally hidden in the rectangular region formed by the dilatation D-modes and the Maxwell eigenvalues. Within the plotted bounds, there is only one branch of discretization X-modes, which contrasts with Fig. 6. On the other hand, the X-branch interferes with the M1, M2 and C0 branches for higher angular orders.

Figure 7. The eigenspectrum of the realistic Earth model (PREM for the density and elastic parameters) with the continuously changing viscous profile in the range from 10^{19} Pa s in the asthenosphere up to more than 10^{23} Pa s in the mid lower mantle, discretized on the grid of 300 Chebyshev layers. The PS scheme has been employed. The classical relaxation modes (M0, L0, C0, M1 and M2) are present but occasionally hidden in the rectangular region formed by the dilatation D-modes and the Maxwell eigenvalues. Within the plotted bounds, there is only one branch of discretization X-modes, which contrasts with Fig. 6. On the other hand, the X-branch interferes with the M1, M2 and C0 branches for higher angular orders.

Table 1. Computational Times for the Eigenproblem (88) per Spherical Harmonic Degree n

Number of grid layers	Matrix dimension	CPU time [s] (Pentium 1 GHz)
30	186^2	0.05
60	366^2	0.4
120	726^2	3
240	1446^2	25
300	1806^2	50